POLITECNICO DI TORINO
Repository ISTITUZIONALE

Size-dependent fracture behavior of quasi-Brittle materials: A peridynamic approach within Ansys LS-DYNA

Original
Size-dependent fracture behavior of quasi-Brittle materials: A peridynamic approach within Ansys LS-DYNA / Ferreira Friedrich, L., Bergamini Puglia, V., Bordin Colpo, A., Iturrioz, I., Lacidogna, G., Madenci, E.. - In: ENGINEERING FRACTURE MECHANICS. - ISSN 0013-7944. - STAMPA. - 342:(2026), pp. 1-26. [10.1016/j.engfracmech.2026.112234]

Availability:
This version is available at: 11583/3013231 since: 2026-07-17T08:53:33Z

Publisher:
Elsevier

Published
DOI:10.1016/j.engfracmech.2026.112234

Terms of use:

This article is made available under terms and conditions as specified in the corresponding bibliographic description in the repository

Publisher copyright

(Article begins on next page)

11 September 2026

Engineering Fracture Mechanics 342 (2026) 112234

Contents lists available at ScienceDirect

Engineering Fracture Mechanics

journal homepage: www.elsevier.com/locate/engfracmech

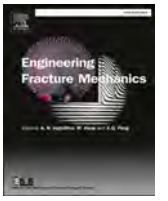

Size-dependent fracture behavior of quasi-Brittle materials: A peridynamic approach within Ansys LS-DYNA

Leandro Ferreira Friedrich [a,*], Vicente Bergamini Puglia [a], Angélica Bordin Colpo [a], Ignacio Iturrioz [b], Giuseppe Lacidogna [c], Erdogan Madenci [d]

[a] Department of Mechanical Engineering, Federal University of Pampa, Av. Tiaraju 810, Alegrete CEP 97546-550, Brazil
[b] Mechanical Post-Graduate Program, Federal University of Rio Grande do Sul, Sarmento Leite 425, Porto Alegre CEP 90050-170, Brazil
[c] Department of Structural, Geotechnical and Building Engineering, Politecnico di Torino, 24, Corso Duca degli Abruzzi, 10129 Torino, Italy
[d] Aerospace and Mechanical Engineering Department, The University of Arizona, Tucson, AZ 85721, USA

ARTICLE INFO

Keywords:
Peridynamics
Finite element
Size-effect
Quasi-brittle materials
Ansys LS-DYNA

ABSTRACT

The transition from toughness-controlled to strength-controlled fracture with changing specimen size – known as the size effect (SE) – is a key feature of quasi-brittle materials. While widely investigated through experiments and conventional numerical models, studies employing Peridynamics (PD) to capture this phenomenon remain scarce and often yield limited accuracy. This work addresses that gap by analyzing the size-dependent fracture behavior of quasi-brittle materials using Bond-Based (BB) PD theory implemented with native elements in Ansys LS-DYNA (PD-DYNA). A novel combination of a bilinear PD model, a 3D stochastic field to represent material heterogeneity, a spatial attenuation kernel, and a discretized micro-modulus function is proposed. The model is validated against two experimental campaigns involving three-point bending tests on notched concrete beams under both mode-I and mixed-mode conditions. Simulations successfully reproduce peak loads, softening behavior, and kinked crack paths observed experimentally. To quantify the scale effect, a fractal-based framework is employed, enabling a consistent interpretation of the mechanical response across specimen sizes. The results demonstrate that the proposed PD-DYNA model can accurately capture the size effect in quasi-brittle fracture, overcoming limitations of earlier PD approaches and validating the potential of fractal-based analysis in PD modeling.

1. Introduction

A persistent challenge in structural engineering lies in accurately translating the mechanical behavior observed in small-scale laboratory tests into reliable predictions for full-scale structures. This issue is particularly relevant for quasi-brittle materials, whose failure mechanisms are sensitive not only to material properties but also to the physical dimensions of the structure, known as the size effect phenomenon [1–3]. Since laboratory specimens are typically several orders of magnitude smaller than real-world

* Corresponding author.
E-mail addresses: leandrofriedrich@unipampa.edu.br (L. Ferreira Friedrich), vicentepuglia@unipampa.edu.br (V. Bergamini Puglia), angelicacolpo@unipampa.edu.br (A. Bordin Colpo), ignacio.iturrioz@ufrgs.br (I. Iturrioz), giuseppe.lacidogna@polito.it (G. Lacidogna), madenci@email.arizona.edu (E. Madenci).

https://doi.org/10.1016/j.engfracmech.2026.112234
Received 1 December 2025; Received in revised form 25 April 2026; Accepted 2 May 2026
Available online 7 May 2026
0013-7944/© 2026 The Author(s). Published by Elsevier Ltd. This is an open access article under the CC BY license (http://creativecommons.org/licenses/by/4.0/).

Nomenclature

a_0	Initial crack length
a_c	Critical crack length
A_f	Cross-sectional area of the beam ligament
b	Beam thickness
$\boldsymbol{b}$	External body force density vector
c	Micro-modulus
$c(0,\delta_0)$	Concentration function for bond stiffness at zero distance
$C_{\sigma u}$, C_{Gf},$C_{\varepsilon u}$	Dimensional constants in the BPD scaling relations
dV	Infinitesimal volume
d	Fractal exponent for a given mechanical property
D_σ, D_ϕ,D_G	Fractal dimension for strength, rotation, and fracture energy
D_eD	Damage parameterFractal dimension
E	Young's modulus
f	Bond force
$\boldsymbol{f}$	Pairwise force density vector
$g(\boldsymbol{\xi},\delta_0)$	Spatial distribution function
G_f	Energy release rate (or fracture energy)
H	Characteristic structural size (beam depth)
h	Thickness of the specimen
K_r	Governs the shape of the softening path
K_{ij}^{PD}	PD spring constant between nodes i and j
l_{cx}, l_{cy}, and l_{cz}	Correlation lengths
L	Beam length
n_f	Brittleness number
$P_{\max}$	Peak load
q_c	Critical loading in the dimensional scaling framework
r	Box side length
s	Bond stretch
s_0	Critical bond stretch
s_p	Maximum elastic stretch
s_r	Rupture stretch
S	Beam span length
t	Time step
$\boldsymbol{u},\boldsymbol{u}'$	Displacement vectors
V	Volume
W	Dissipated energy (area under force–CMOD curve)
$\boldsymbol{x},\boldsymbol{x}'$	Position vectors in the undeformed configuration
Y	Geometric shape function
Z	Characteristic size in brittleness number
α	Notch-to-depth ratio
β	Notch eccentricity
δ_0	Numerical Peridynamic horizon
δ_c	Beam vertical displacement
δ'	Horizon characteristic material length
Δ	Grid spacing
ε_u	Critical strain
$\boldsymbol{\eta}$	Relative displacement vector
λ	Volume correction factor
$\boldsymbol{\xi}$	Relative position vector
$\widehat{\mu}$	Bond status parameter
ν	Poisson's ratio
ρ	Mass density
σ_0	Failure stress of the material under tension
σ_N	Flexural strength
ϕ	Rotation angle
φ	Local damage index
BB PD	Bond-based peridynamics

BPD	Bilinear Peridynamics material model
CTOD	Crack tip opening displacement
CMOD	Crack mouth opening displacement
CV_{Gf}	Coefficient of variation for G_f
CZM	Cohesive Zone Model
DG	Discontinuous Galerkin
FPZ	Fracture Process Zone
LC, ULC	Loading and Unloading Curve
LDEM	Lattice Discrete Element Method
LEFM	Linear Elastic Fracture Mechanics
PFM	Phase Field Method
PMB	Prototype Microelastic Brittle model
PD	Peridynamics
PD-DYNA	Coupled Peridynamics/LS-DYNA
SEL	Size Effect Law
TYI, CYI	Maximum and minimum force in LC
XFEM	Extended Finite Element Method

components, direct extrapolation of strength or fracture properties often leads to inaccurate or non-conservative designs. Large-scale experimental campaigns, while ideal, are often impractical due to their high cost and complexity [4]. As such, the development of computational models capable of predicting how mechanical behavior evolves with structure size is both a theoretical necessity and an engineering priority.

The structural size effect is a phenomenon especially pronounced in quasi-brittle materials such as concrete, rock masses, sea ice bodies, fiber–polymer composites, and ceramics which exhibit failure through a gradual accumulation of damage, micro cracking, and energy dissipation within a finite region known as the Fracture Process Zone (FPZ) [5]. Unlike fully brittle materials, which fail abruptly at a critical stress, or ductile materials, which accommodate large plastic strains, quasi-brittle materials display a mixed failure mode that cannot be captured by simple strength-based or toughness-based criteria alone.

To account for the size dependence of fracture in such materials, classical theories like the Size Effect Law (SEL) have been developed [1,6]. The SEL provides a framework for capturing the transition from ductile-like strength control at small scales to brittle-like energy control at large scales, based on principles from Linear Elastic Fracture Mechanics (LEFM). This law has been widely applied and validated across different material systems and structural geometries [7]. However, some authors [4,8,9] have reported that, in situations where the specimen boundaries limit the expansion of the fracture process zone (FPZ), the conventional SEL may not preserve high local accuracy.

An alternative perspective that has gained attention in recent years is the fractal interpretation of the size effect proposed by Carpinteri and coworkers [10,11], named in the following as fractal size effect. Experimental observations suggest that fracture surfaces in quasi-brittle materials often exhibit self-similar or self-affine geometries, characterized by non-integer fractal dimensions [12]. From this point of view, the reduction in strength with increasing structure size may not arise especially from energetic considerations, but also from the increasing roughness and geometrical complexity of the crack path. This fractal size effect introduces a fundamentally different explanation, rooted in the geometry of the fracture surface rather than the scaling of energy dissipation zones. To rigorously test this hypothesis, computational methods must be capable of capturing complex crack patterns, roughness evolution, and size-dependent behavior in a natural and unified framework. As a matter of fact, evaluating the size effect in quasi-brittle materials is now considered a fundamental benchmark for quantitatively validating computational fracture models [13].

In recent years, a wide range of numerical approaches have been developed to investigate fracture phenomena and capture size effects in brittle and quasi-brittle materials. These approaches can be broadly classified into two main groups: models based on continuum mechanics and models that explicitly account for the random nature of the material microstructure.

Models based on continuum mechanics extend classical solid mechanics to accommodate crack initiation and growth. Examples include the Cohesive Zone Model (CZM) [14–16], originally proposed for pre-cracked solids and later adapted to intact structures; the Smeared Crack Model [17], often coupled with the crack band model [16] to prevent mesh-dependent localization by introducing a characteristic length [18]; and the Extended Finite Element Method (XFEM) [19], which enriches the displacement field to represent discontinuities without remeshing. The Phase Field Method (PFM) [20,21] represents cracks through a continuous damage variable, eliminating the need for explicit crack tracking and enabling the modeling of complex fracture processes. While PFM provides mesh-objective results through the introduction of a length scale, it is often sensitive to the choice of this parameter and generally requires fine discretization.

Models that account for the random nature of the microstructure include discrete approaches such as the Lattice Discrete Element Method (LDEM) [22,23], in which the material is represented by a network of truss or beam elements with mass concentrated at their nodes. These models explicitly incorporate the stochastic heterogeneity of materials, making them particularly suitable for studying damage processes in detail, including crack initiation, propagation, interaction, and branching. They have also demonstrated consistency with fractal interpretations of size effects, providing a valuable framework for investigating how structural dimensions influence fracture behavior [24,25].

An alternative to the above approaches is offered by models based on the Peridynamic (PD) theory [26]. As a nonlocal

reformulation of continuum mechanics, PD enables the simulation of fracture without the need for additional criteria to handle discontinuities. Its integral-based formulation allows for the modeling of crack initiation, propagation, branching, and coalescence, making it particularly suitable for studying quasi-brittle failure across multiple scales. Although PD has been increasingly applied to model fracture in quasi-brittle materials, few studies have specifically addressed the structural size effect using this approach. Hobbs et al. [27] modeled geometrically scaled beams with a 3D PD formulation with an exponential pairwise force function, comparing the results with the classical SEL. However, Bažant et al. [28] questioned the capability of PD to accurately reproduce the transitional size effect typical of quasi-brittle fracture. However, Bazilevs et al. [29] introduced the Microplane model (M7) of concrete into the non-ordinary state-based PD formulation. This constitutive model captures size effects with additional parameters to account for concrete's complex mechanical behavior. Previous work [30] by a few of the present authors investigated the fractal size effect using a Bond-Based (BB) PD model with a bilinear PD model and a 3D stochastic field for the energy release rate, applied to unnotched beams of expanded polyethylene (EPS). The results supported the fractal interpretation and showed good agreement with experimental data. These findings suggest that, while PD holds promise for simulating complex fracture processes, its application to size effect problems remains limited and requires further refinement.

In the context of PD analysis capability in LS-DYNA, Ren et al. [31] treated the integration points in Discontinuous Galerkin (DG) elements as PD points. Therefore, the PD bond kinematics is dictated by the integration points in DG element. However, it allows discontinuity only along the inter-element boundaries. Consequently, damage path is dependent on the FE discretization and remeshing within the element is required to capture accurate damage path. Damage occurs only along element boundaries and cannot propagate through the element. If the bonds at a PD point are partially broken within the element, the element displacement field cannot account for such discontinuities.

In this context, the present study investigates the size-dependent fracture behavior of quasi-brittle materials by using the PD theory integrated into the explicit dynamic environment of Ansys LS-DYNA, referred to here as PD-DYNA [32]. The model is based on BB PD, incorporating several key features that enhance its ability to represent real material behavior. These include a bilinear PD model to capture stiffness degradation and failure, a three-dimensional stochastic field to represent material heterogeneity, a spatial attenuation kernel to reflect the decaying influence of distant bonds, and a discretized micro-modulus function that ensures consistency with classical elastic properties. The framework has been validated against two experimental datasets involving three-point bending tests on notched concrete beams, covering both mode I [33] and mixed-mode fracture [34] conditions. Both experimental and numerical results are compared in terms of global behavior, brittleness, failure configuration and the fractal size effect on the flexural strength, critical rotation angle and critical energy release rate (fracture energy). It is worth noting that the fractal framework adopted here is not used as a constitutive assumption nor as a calibration tool. Instead, it serves only as an interpretative framework to quantify the

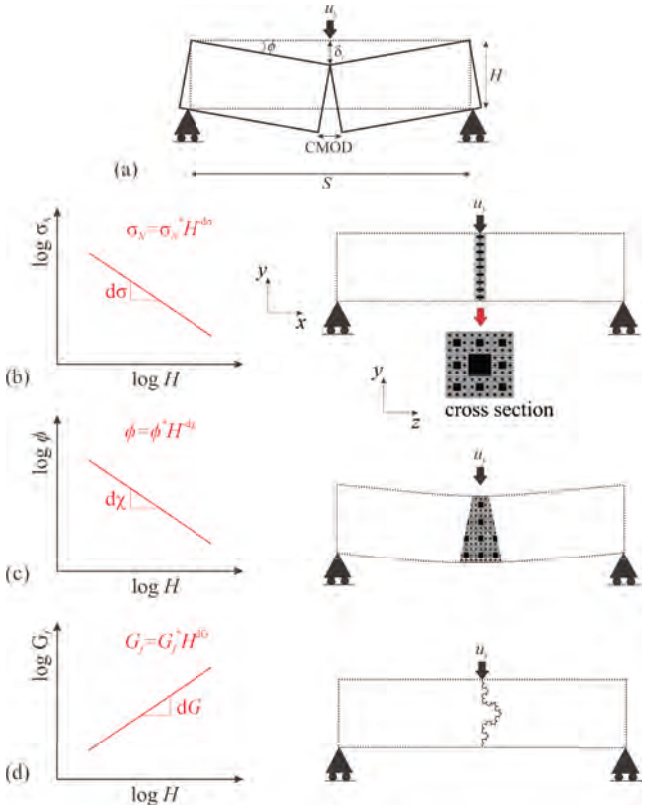

Fig. 1. Summary of the power laws that represent the scale effect of flexural strength (d_σ), angle of rotation ($d\chi$) and fracture energy (d_G).

scaling trend of the above mechanical properties.

2. The fractal size effect

Carpinteri and co-workers [10,11,35] proposed that fractal geometry offers a unified explanation for the scale effects on the mechanical properties of quasi-brittle materials. In fact, experimental evidence confirms that on the fracture surface of many materials, fractal shapes can be observed, such as in metals, ceramics, concrete, rocks, among others [36]. According to Lacidogna et al. [37], three mechanical properties, flexural strength, critical rotation angle and fracture energy, that are size-dependent can be evaluated from three-point bending tests. In general, the measurement of the variation of a given mechanical property above (Q) is performed through the so-called fractal exponents, dQ, described by a power law as:

$$Q = Q^{*} H^{dQ} \tag{1}$$

where Q^{*} is the scale invariant material property and H a characteristic dimension of the structure. Fig. 1 summarizes the scale effect of these properties described by power laws indicated in the bi-log domain, where $d\sigma$, $d\chi$ and d_G are the fractal exponents of the flexural strength (σ_N), critical angle of rotation (ϕ) and energy release rate (or fracture energy) (G_f), respectively. These mechanical quantities are computed as (see Fig. 1(a)):

$$\sigma_N = \frac{3P_{\max} S}{2tH^2} \tag{2}$$

$$\phi = \frac{CMOD_{P\max}/2}{H} = \frac{\delta_c}{S/2} \tag{3}$$

$$G_f = \frac{W}{A_f} \tag{4}$$

where $P_{\max}$ is the peak load, $CMOD_{P\max}$ is the crack mouth opening displacement at peak load, δ_c the vertical displacement at the center of the beam at peak load, A_f the cross-section beam area considering the notch depth and W the dissipated energy, computed as the area of the Force $-$ $CMOD$ curve. It is worth noting that the dissipated energy is evaluated from the Force–CMOD curve rather than from the force $-$ vertical displacement curve. In notched three-point bending tests, the CMOD provides a direct measurement of the crack opening at the notch tip and therefore isolates the energy consumed by the fracture process within the ligament. This definition is consistent with established experimental protocols for determining the fracture energy of quasi-brittle materials [38].

It is worth noting that according to the fractal size effect theory, the flexural strength develops over a ligament area with a fractal dimension given by $D_\sigma = 2 - d\sigma$, that is smaller than a Euclidean surface, due to defects and heterogeneities. Lacunar sets, such as the Cantor set, can represent this discontinuous load-bearing domain (Fig. 1(b)). Similarly, the critical rotation angle scales with size over a deformation domain of fractal dimension $D_\phi = 1 - d\phi$, reflecting the localized and discontinuous strain distributions within the ligament (Fig. 1(c)). Fracture energy dissipates over a rough crack domain with a fractal dimension $D_G = 2 + dG$, representing the complex topology of micro cracks. As a result, G_f scales with size according to the measure of this fractal domain, deviating from classical LEFM predictions. From a fractal point of view, invasive fractal sets, such as the von Koch triadic curve, can be used to represent it (Fig. 1(d)).

The range of variations observed in fractal exponents depends on several factors, including the geometrical shape of the specimens, the boundary conditions, the material characteristics, and other variables. According to the studies by Lacidogna et al. [37] and Carpinteri and Accornero [39], the exponent values typically range from 0.1 to 0.3 for flexural strength, 0.2 to 0.5 for the critical rotation angle and 0.1 to 0.3 for fracture energy. It is important to note that the fundamental link between the fractal exponents follows from an energy balance written in natural dimensionless variables as detailed in [30,37,39]. More precisely, it is based on

$$d\sigma + d\chi + dG = 1 \tag{5}$$

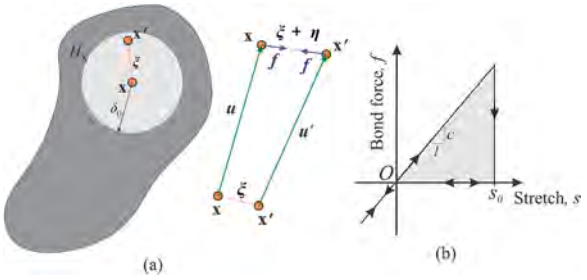

Fig. 2. A) peridynamic continuum, kinematics of pd points $\boldsymbol{x}$ and $\boldsymbol{x}'$ and bond-based pairwise force function, and b) Prototype Microelastic Brittle (PMB) material model.

This relation expresses the self-similar redistribution of strength, rotation angle and fracture energy across scales.

3. Peridynamic formulation for Quasi-Brittle materials

3.1. BB-PD theory with improved micro-elastic modulus

This section presents a concise overview of the BB-PD theory. For further details, please refer to classic references such as Silling [26], Silling and Askari [40], and Madenci and Oterkus [41].

Fig. 2a illustrates the kinematics of PD interactions (bonds) between material points. The deformed configuration of a body is described by the position of material points with each point having a family populated by other points within its horizon, δ_0. The bond force between material point, $\boldsymbol{x}$ and its neighbouring point $\boldsymbol{x}'$ in its horizon is defined by the pairwise force density vector, $\boldsymbol{f}$. It represents the force vector per unit volume exerted by point $\boldsymbol{x}'$ on point $\boldsymbol{x}$. The direction of this force density vector is aligned with the direction of the bond in the deformed configuration as shown in Fig. 2a.

The PD form of the equation of motion, at a given time step t, is derived as [26]

$$\rho\ddot{\boldsymbol{u}}(\boldsymbol{x},t)=\int_{H_x}\boldsymbol{f}(\boldsymbol{x}'-\boldsymbol{x},\boldsymbol{u}'-\boldsymbol{u})dV_{x'}+\boldsymbol{b}(\boldsymbol{x},t) \tag{6}$$

where ρ is the material mass density, $\boldsymbol{x}$ and $\boldsymbol{x}'$ are the position vectors, $\boldsymbol{u}$ and $\boldsymbol{u}'$ are the displacement vectors, $dV_{x'}$ denotes an infinitesimal volume of the point $\boldsymbol{x}'$ and $\boldsymbol{b}$ is the external body force density vector. The force density vector associated with nonlocal interactions, denoted by $\boldsymbol{f}$, plays a central role in accurately describing the mechanical response of materials within the peridynamic framework. A first model in this context is the Prototype Microelastic Brittle (PMB) model (Fig. 2b), originally introduced by Silling and Askari [40], which was developed for the analysis of isotropic materials. In this model, the material is considered to be stress-free in its undeformed configuration, meaning that the initial bond force density is zero. The interaction force between two material points is modelled as a pairwise force, conceptually similar to a spring (bond), and is defined as:

$$\boldsymbol{f}=\widehat{\mu}cs\frac{\boldsymbol{\xi}+\boldsymbol{\eta}}{|\boldsymbol{\xi}+\boldsymbol{\eta}|} \tag{7}$$

where $\boldsymbol{\xi}=\boldsymbol{x}'-\boldsymbol{x}$ is the relative position vector, $\boldsymbol{\eta}=\boldsymbol{u}'-\boldsymbol{u}$ is the relative displacement vector, $s=|\boldsymbol{\xi}+\boldsymbol{\eta}|-|\boldsymbol{\xi}|/|\boldsymbol{\xi}|$ is the bond stretch, and c is the micro-modulus. The original PMB model, employs a constant micro-elastic modulus, which does not account for the distance-dependent attenuation of nonlocal interactions. This simplification limits the model's ability to capture the realistic spatial distribution of the bonds. To address this issue, several studies have proposed modified PMB constitutive formulations incorporating attenuation kernel functions that introduce spatial variability into the bond stiffness [42–45]. In the present work, an improved PMB model is adopted in which the micro-elastic modulus function is defined as

$$c(\boldsymbol{\xi},\delta_0)=c(0,\delta_0)g(\boldsymbol{\xi},\delta_0) \tag{8}$$

where $c(0,\delta_0)$ is a concentration function that describes the stiffness of the pairwise bond of two material points approaching zero distance, and $g(\boldsymbol{\xi},\delta_0)$ is the quartic polynomial kernel function or spatial distribution function [42,45], both defined as,

$$g(\boldsymbol{\xi},\delta_0)=\begin{cases}\left(1-\left(\dfrac{|\boldsymbol{\xi}|}{\delta_0}\right)^2\right)^2 & \text{if}\quad |\boldsymbol{\xi}|\leqslant\delta_0\\ 0\ \text{if}\quad |\boldsymbol{\xi}|>\delta_0\end{cases} \tag{9a}$$

and

$$c(0,\delta_0)=\begin{cases}\dfrac{36E}{\pi\delta_0^4(1-2\nu)} & \text{3D analysis}\\ \dfrac{105E}{4\pi h\delta_0^3(1-\nu)} & \text{2D analysis} - \text{ plane stress}\\ \dfrac{105E}{4\pi h\delta_0^3(1-2\nu)(1+\nu)} & \text{2D analysis} - \text{ plane strain}\end{cases} \tag{9b}$$

where E is the elastic modulus, h is the thickness and δ_0 is the horizon of material points (assumed to be uniform). The Poisson's ratio has a value of $\nu=0.25$ for 3D dimensional analysis and 2D analysis under plane strain conditions whereas it is fixed as $\nu=0.33$ for 2D analysis under plane stress conditions [26,40].

When a material point is located near a boundary or a bi-material interface, its interaction domain becomes truncated or directionally biased due to the use of an idealized circular or spherical horizon. This asymmetry leads to reduced accuracy in the calibration of micro-modulus values compared to points located within the bulk of the material. As a result, the predicted deformation and fracture behavior in boundary regions may be compromised—an issue commonly referred to as the surface effect. To account for this, the micro-elastic modulus of the boundary region is computed as,

$$c_i(\boldsymbol{\xi},\delta_0)=\begin{cases}\dfrac{6E}{(1-2\nu)\sum_{j\in H_i}\left(1-\left(\frac{|\boldsymbol{\xi}|}{\delta_0}\right)^2\right)^2|\boldsymbol{\xi}_{ij}|V_j} & \text{3D analysis}\\ \dfrac{4E}{(1-\nu)\sum_{j\in H_i}\left(1-\left(\frac{|\boldsymbol{\xi}|}{\delta_0}\right)^2\right)^2|\boldsymbol{\xi}_{ij}|V_j} & \text{2D analysis} - \text{ plane stress}\\ \dfrac{4E}{(1-2\nu)(1+\nu)\sum_{j\in H_i}\left(1-\left(\frac{|\boldsymbol{\xi}|}{\delta_0}\right)^2\right)^2|\boldsymbol{\xi}_{ij}|V_j} & \text{2D analysis} - \text{ plane strain}\end{cases} \tag{10}$$

However, the discretized horizons of the two material points associated with a bond are different. To preserve the symmetry of the interaction and ensure that the bond force satisfies the condition of linear momentum balance ($\boldsymbol{f}_{ij}=\boldsymbol{f}_{ji}$), the arithmetic average of micro-modulus of point $\boldsymbol{x_i}$ and point $\boldsymbol{x_j}$ is adopted for a bond between these material points as:

$$c_{ij}=\frac{c_i+c_j}{2} \tag{11}$$

In Eq. (7) if the stretch reaches its critical value, s_0, the status parameter $\widehat{\mu}$ takes on a value of 0, otherwise, it remains as 1, that is,

$$\widehat{\mu}=\begin{cases}1 & \text{if} \quad s<s_0\\ 0 & \text{if} \quad s\geqslant s_0\end{cases} \tag{12}$$

in which s_0 can be evaluated as [32,40]

$$s_0=\sqrt{\frac{RG_f}{E\delta_0}} \tag{13}$$

where G_f is the material energy release rate and R is equal to 5/6 for 3D analysis, and $4\pi/9$ and $5\pi/12$ for 2D plane stress and plain strain analysis, respectively. A local damage index φ, which can be used to define the crack path, can be defined as

$$\varphi(\boldsymbol{x},t)=1-\frac{\int_{H_x}\widehat{\mu}dV_{x'}}{\int_{H_x}dV_{x'}} \tag{14}$$

It is simply ratio of number of broken bonds to the total number of bonds at point $\boldsymbol{x}$.

3.2. A peridynamic approach for quasi-brittle materials

The PD approach proposed by Friedrich et al. [46] is employed in order to perform the failure analysis of quasi-brittle materials. The main features of this approach are the implementation of: (i) a bilinear bond force-stretch relationship, and (ii) a random field for

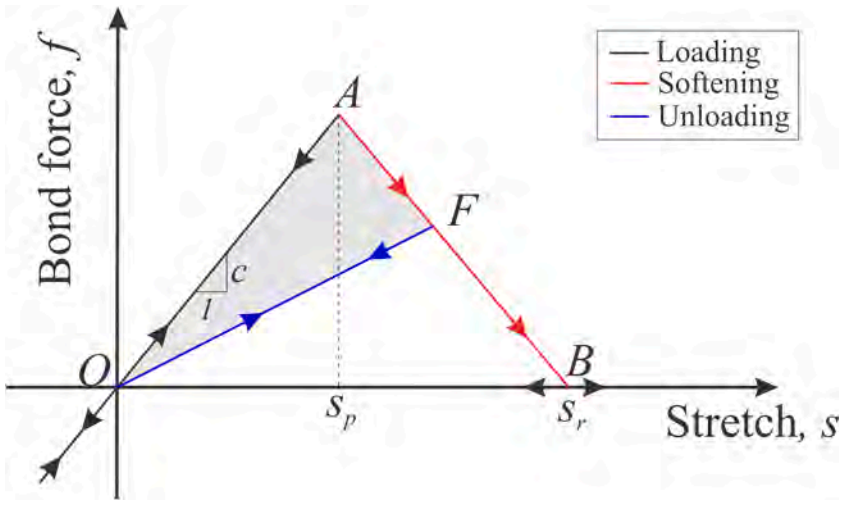

Fig. 3. Bond force-stretch relationship in BPD model for quasi-brittle material behaviour.

the energy release rate.

The Bilinear PD (BPD) material model was initially introduced by Cabral et al. [47] and further improved by Friedrich et al. [46]. The model exploits two sizes for the horizon, and more precisely:

the size δ_0, defined in the previous sub-section, assumed to be equal to $\delta_0 = m\Delta$ with $m = 3.015$, called computational horizon and the size δ', assumed as a material characteristic (it will be defined in the following).

The main advantage of the BPD material model is its correlation between δ' and δ_0, which allows simulating the same global material behaviour with different levels of grid spacing, Δ. This allows reducing computation time significantly. In Cabral et al. [47] and Friedrich et al. [46] several numerical results obtained with the present model were compared with experimental ones, showing the capabilities of such a model. Moreover, recently, versions of the BPD material model taking into account shear effects and the fatigue degradation process were proposed by Friedrich et al., [48] and Friedrich et al., [49], respectively.

3.2.1. Bilinear PD (BPD) model formulation

The bilinear bond force-stretch relationship is shown in Fig. 3. Three main parameters characterise such a relationship:

(1) the slope of loading path, that is the micro-modulus, c (Eq. (8) or (11))
(2) the maximum elastic stretch, s_p, computed as:

$$s_p = \frac{\sigma_0}{E} \tag{15}$$

where σ_0 is the failure stress of the material under tension. It is worth noting that Eq. (15) is valid for cases where the material exhibits near linear behaviour up to failure. In cases of significant nonlinearity before fracture, such an assumption should not be considered. In such cases, s_p can be assumed as the strain at which the linear behaviour of the structure is lost; it comes from experimental data, such as stress–strain or stress-displacement curves. The detailed explanation can be found in Friedrich et al. [46].

(3) the rupture stretch, s_r, defined as:

$$s_r = K_r s_p \tag{16}$$

where K_r governs the shape of the softening path (red line in Fig. 3). In order to obtain the relationship to compute K_r, firstly the area underlying the PMB bond force-stretch relationship (see Fig. 2b) is equated to that of the BPD bond force-stretch relationship (Fig. 3) as

$$s_0^2 = s_p s_r = K_r s_p^2 \tag{17}$$

Replacing δ_0 with δ' in Eq. (13), for the critical stretch corresponding to the PMB model, yields the value for s' as

$$s' = \sqrt{\frac{RG_f}{E\delta'}} \tag{18a}$$

or

$$(s')^2\delta' = \frac{RG_f}{E} \tag{18b}$$

and by replacing s_0 from Eq. (13) and Eq. (18b) into Eq. (17), the following relation is obtained

$$K_r s_p^2 \delta_0 = (s')^2\delta' \tag{19}$$

When $\delta' = \delta_0$, BPD model recovers the PMB model originally proposed by Askari and Silling [40]; thus, the BPD model can be considered as a generalization of the PMB model.

For the BPD material model, the degradation in the bond force can be written as:

$$f = c(1 - D_e)s \tag{20}$$

where D_e is a damage parameter. It can be defined as

$$D_e = \begin{cases} 0 & \text{for } s \leqslant s_p \\ \dfrac{s - s_p}{s}\dfrac{s_r}{s_r - s} & \text{for } s_p < s \leqslant s_r \\ 1 & \text{for } s > s_r \end{cases} \tag{21}$$

In accordance with Eq. (12), the local damage measure, φ can be rewritten asφ = 1-D_e.

3.2.2. The physical meaning of the material characteristic horizon (δ')

Different strategies exist in the literature to determine the material characteristic horizon δ'. For instance, Friedrich et al. [46]

employed the Theory of Critical Distances (TCD) [50] to link δ' to the material critical distance L_E. In the present study, δ' is defined by exploiting the concept of stress brittleness number; it is based on the original formulation of the BPD model [46]. This approach not only provides a clear physical interpretation of δ' as material characteristic length but also establishes a direct connection with a critical crack length and the structural size effect.Concepts from Linear Elastic Fracture Mechanics (LEFM) can employed to assign a physical meaning to δ'. Considering Eq. (18b) and the relation between the critical stress intensity factor, K_{Ic}, and the energy release rate, G_f, (i.e., $G_f = K_{Ic}^2/E$, under plane stress assumption) yields the expression for δ' as

$$\delta' = \frac{R}{(s')^2}\left(\frac{K_{Ic}}{E}\right)^2 \tag{22}$$

For a crack under Mode I loading, the critical crack length at failure can be determined as $a_c = \frac{1}{\pi}\left(\frac{K_{Ic}}{\sigma_0 Y}\right)^2$ and assuming the applied load is $\sigma_0 = Es'$, evaluation of Eq. (22) leads to

$$\delta' = RY^2\pi a_c \tag{23}$$

where Y is the geometric shape function, which depends on the geometry and boundary conditions of the cracked body. It should be noted that the present analysis focuses on the scale of material defect nucleation and internal force interactions; therefore, the influence of the global structural geometry and boundary conditions can be considered as secondary importance. In this context, assuming $R\sqrt{Y\pi} \approx 1$ in Eq. (23) results in $\delta' = a_c$. This indicates that the material characteristic horizon δ' can be directly interpreted as the size of a potential critical crack embedded in the material leading to unstable crack growth once the local stress reaches a critical level. A detailed discussion of this interpretation within the peridynamic framework can be found in Cabral et al. [47]. Similar concepts have also been employed in other discrete methods [24,25,51].

The concept of the stress brittleness number, n_f, proposed by Carpinteri [52] can be adopted to generalize the determination of δ' for arbitrary structural geometries and to quantify the size-dependent transition between ductile and brittle failure. This dimensionless number quantifies the degree of brittleness or ductility of a structure and describes how this quality depends on the characteristic structural dimension. It has been widely employed by researchers in various fields of applied mechanics to characterize different aspects of the size effect phenomenon (see, e.g., Gao [53]).

The stress brittleness number is defined in terms of energy release rate as

$$n_f = \frac{(G_f E)^{0.5}}{\sigma_0\sqrt{Z}} \tag{24}$$

where Z is a characteristic structural dimension (e.g., the beam depth). By combining Eqs. (18b) and (24), the parameter δ' can be computed as

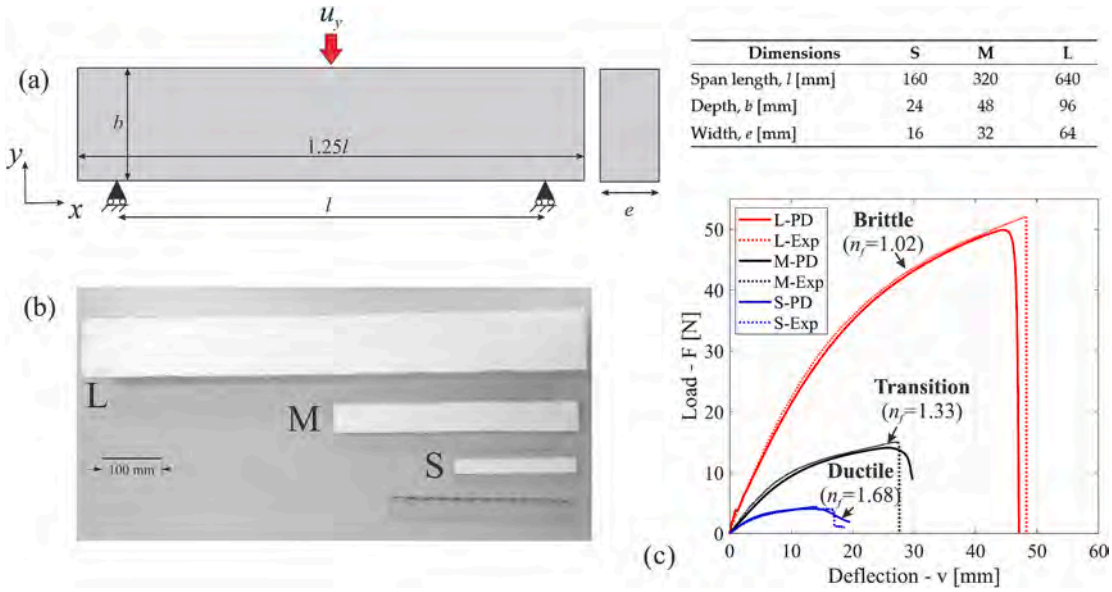

Dimensions	S	M	L
Span length, l [mm]	160	320	640
Depth, b [mm]	24	48	96
Width, e [mm]	16	32	64

Fig. 4. EPS beams under three point bending testing considered by Friedrich et al. [30] (a) beams dimensions named as Large (L), Medium (M), and Small (S), (b) Relative size of the EPS specimens, and (c) Representative numerical PD results and experimental measurements in terms of load–deflection curves in order to show the ductile-to-brittle transition behavior based on the stress brittleness number.

$$\delta' = n_f^2 RZ \tag{25}$$

It is important to emphasize that δ' is a material parameter, independent of the specimen geometry. Once the material properties G_f, E and σ_0 are known, they directly reflect the toughness, stiffness, and strength of the material, respectively. In contrast, Z is a structural characteristic length (e.g., the beam depth, H).

Equation (25) captures the deterministic aspect of the size effect: it relates the dimension in which elastic energy is stored within the structure to the dimension in which this energy is dissipated when an embedded critical crack propagates unstably. In other words, the ratio between the material length scale (δ') and the structural size (Z) governs the ductile-to-brittle transition captured by the brittleness number (n_f). It is also worth noting that this deterministic scaling interacts with the statistical size effect, which arises because larger specimens have a higher probability of containing both weaker and stronger local regions due to material heterogeneity. The random G_f field introduced in Section 3.2.3 accounts for this statistical variability. Together, the deterministic length-scale competition (via δ' and Z) and the stochastic strength distribution (via the random field) dictate the global failure behaviour, including localization, collaborative effects, and the observed scatter in experimental results.

Based on experimental data and numerical simulations, values of $n_f > 1.5$ indicate ductile (strength-controlled) fracture, whereas $n_f < 1.0$ corresponds to brittle (LEFM-controlled) fracture [25,52]. Consequently, by comparing the fixed material horizon δ' with the variable structural size Z, the BPD model naturally predicts the ductile-to-brittle transition without any further parameter adjustment. This is one of the major advantages of bilinear PD formulation.

A comprehensive parametric study on the influence of δ' (and thus of the brittleness number n_f) on the global load-displacement response using 3D PD models was carried out by Friedrich et al. [30] for Expanded PolyStyrene (EPS) beams of different sizes subjected to three-point bending. Fig. 4a shows the dimensions of the Large (L), Medium (M), and Small (S) beams, together with their corresponding brittleness numbers. Fig. 4b shows relative size of the EPS specimens. With $\delta' = 40$ mm (computed from the material properties G_f, E and σ_0 , taking the beam depth as the characteristic structural dimension Z), the predictions shown in Fig. 4c (dotted lines represent experimental results for comparison) capture the following:

- The L beam ($Z \gg \delta'$, $n_f \approx 1.0$) exhibits a brittle failure, as the structure can fully contain the critical crack size δ'.
- The S beam ($Z < \delta'$, $n_f > 1.5$) exhibits a ductile failure, because the structural size is insufficient to accommodate a critical crack of length δ'.
- The M beam ($Z \approx \delta'$, $1.0 < n_f < 1.5$) shows a transitional quasi-brittle response.

This example clearly illustrates how the specified material parameter δ', when combined with the geometry-dependent brittleness number n_f, enables the BPD model to capture the full spectrum of size-dependent fracture behavior in quasi-brittle materials.

By combining Eq. (18a) with Eq. (19) and considering the definition of n_f in Eq. (24) leads to the evaluation of $s' = \sigma_0/E$ which is the same as that of s_p in Eq. (15). Therefore, the parameter K_r in Eq. (19) defines a connection between the computational horizon δ_0 and δ' as

$$\delta' = K_r \delta_0 \tag{26}$$

Therefore, the input data required for the BPD material model shown in Fig. 3 are as follows: the material properties E, G_f, and σ_0; the grid spacing Δ, which defines the discretization; and the characteristic structural dimension, Z. When the maximum elastic stretch s_p is determined directly from experimental data as the strain at which the linear behaviour terminates, it is also provided as an input parameter.

3.2.3. 3D random field of energy release rate

The non-homogeneous nature of engineering materials is accounted in the PD models using random fields. Specifically, a random field for the energy release rate has been implemented. It is essential in predicting crack initiation sites and propagation paths. A three-dimensional field is assumed to have a Weibull probability distribution, defined by the correlation lengths l_{cx}, l_{cy}, and l_{cz}, and the coefficient of variation, CV_{Gf}. Consequently, as the parameters s_p and s_r are functions of G_f, the $f-s$ relationship is different for each bond. The correlation lengths, l_{cx}, l_{cy}, and l_{cz} and CV_{Gf} serve as input data for the G_f random field, as explained in detail by Friedrich et al., [46,48].

3.3. Implementation of peridynamics in Ansys LS-DYNA

This section presents a version of the PD theory implemented in the Ansys LS-DYNA environment (named PD-DYNA in the following), which employs an explicit dynamics solver [54]. This implementation supports simulations using either standalone PD-DYNA or a coupled PD-DYNA/Finite Element Method (FEM) formulation to create hybrid models. Specifically, PD-DYNA is applied to subdomains characterised by discontinuities and fracture-driven material failure, while FEM is used elsewhere.

The PD-DYNA implementation was originally introduced in Friedrich et al. [32]. In the present study, the original formulation is extended by incorporating a spatial attenuation kernel and a discretized micro-modulus function, enabling a more flexible representation of nonlocal interactions. These extensions also allow, for the first time within the PD-DYNA framework, the combined use of a bilinear PD model, a stochastic energy release rate field, a spatial attenuation kernel, and a discretized micro-modulus function.

As mentioned previously, a PD-based approach in LS-DYNA is available in the literature [31]. However, it relies on Discontinuous Galerkin (DG) formulations, in which cracks are restricted to inter-element boundaries and the accuracy depends strongly on the underlying finite element mesh. In contrast, the PD-DYNA or PD-DYNA/FEM formulation used in the present work employs native LS-DYNA elements to represent PD bonds, enabling a fully nodal, mesh-independent description of interactions without DG constraints.

Fig. 5 outlines the workflow for constructing and solving models with the coupled PD-DYNA/FE regions. In the PD-DYNA model, the bonds are modeled by using COMBI165 elements [54]. It has two nodes with only one element between the nodes. It represents an explicit spring-damper system. If the bond interaction forces between nodes i and j as are considered as spring forces, a PD spring constant, K_{ij}^{PD}, can be obtained as

$$K_{ij}^{PD} = \frac{c_{ij}}{\xi_{ij}} \lambda_{ij} V_i V_j \tag{27}$$

where ξ_{ij} represents the length of the PD bond, λ_{ij} is the volume correction factor, V_i and V_j are the corresponding volumes of nodes i and j. For a uniform grid spacing, they are equal to Δ^3.

The volume correction factor in Eq. (27) is applied to improve the accuracy of the midpoint integration method, i.e., the nodal volume/area of node i may not be fully embedded within the horizon of node j. The volume correction factor for a uniform grid can achieved by [55]

$$\lambda_{ij} = \begin{cases} 1 \text{ if } |\xi| \leqslant \delta_0 - \Delta/2 \\ \dfrac{\delta_0 + \Delta/2 - |\xi|}{\Delta} \text{ if } \delta_0 - \Delta/2 \leqslant |\xi| \leqslant \delta_0 + \Delta/2 \\ 0 \text{ if } |\xi| \geqslant \delta_0 + \Delta/2 \end{cases} \tag{28}$$

It is worth noting that each element has a different bond spring constant because of varying volume correction factors, micro-modulus and bond lengths. However, it is possible to achieve a computationally acceptable number of PD bond spring constants through a comparative analysis of the bond lengths, micro-modulus, and volume correction factor.

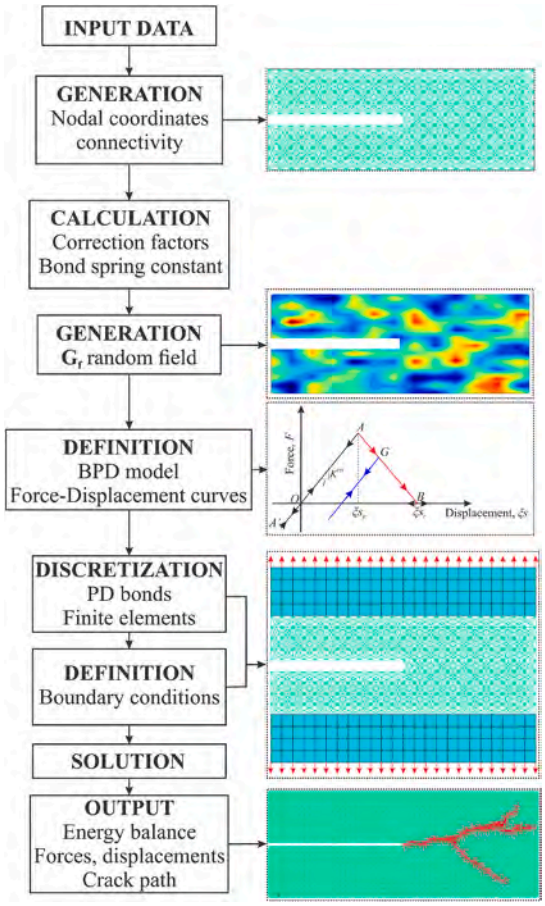

Fig. 5. Schematization of the procedure employed to create a hybrid model, solution and results.

The parameters of the *Bilinear PD model* described in Fig. 3 are defined and converted to a force–displacement relationship. Each bond is represented by a material model within Ansys LS-DYNA. More precisely, the General Nonlinear Spring Model is employed by using the MAT, TB and TBDAT commands as (for a material number k):

```
MAT, k
TB, DISCRETE, k, …5
TBDAT, 1, LC
TBDAT, 2, ULC
TBDAT, 3, 1
TBDAT, 4, TYI
TBDAT, 5, CYI
```

where LC is the loading and ULC is the unloading curves that relate the force versus displacement of the spring (that is "bond"). The points that define LC are *A'-O-A-B* are shown in Fig. 5. The unloading curve (ULC) has the same points as LC. The maximum and minimum bond forces in the LC curve are TYI and CYI with values of $K^{PD}\xi s_p$ and $-K^{PD}\xi s_p$, respectively. It is important to note that in PD-DYNA, unloading occurs in parallel to the loading curve, i.e. with residual strains. In Ansys LS-DYNA, it is not possible to define a material in the absence of residual strains. However, bilinear laws with residual strains in general do not lead to a significant change in the simulation of the global behavior of quasi-brittle materials (Colpo et al. [56]).

The material heterogeneity approach, employed in the BPD material model described in the previous section, is included in a PD-DYNA model as well, that is by means of a random G_f field. See Friedrich et al. [32] for details regarding the random G_f field implementation.

In PD-DYNA, the mass of the body is discretized by using the Explicit 3-D Structural Mass (MASS166) element, with the masses concentrated in the COMBI165 nodes. The mass value is defined by $\rho\Delta^3$ with ρ being the material mass density.

For the FE region, the SOLID164 element is used to perform 3D analyses. However, 2D explicit elements like PLANE162 cannot be used, as Ansys LS-DYNA restricts combining 2D and 3D elements in a single simulation due to the presence of MASS166 elements [54]. As a result, SHELL163 is employed for 2D simulations. The PD-DYNA and FE regions are then connected through coincident nodes, forming a hybrid model. Coupling of degrees of freedom (displacements and rotations) can be achieved using the CP command, while the NUMMRG command allows merging these overlapping nodes [32]. It's important to note that FE nodes interact only within their own elements, whereas PD nodes communicate with neighboring nodes via PD bonds.

4. Size effect for mode I problems

4.1. Experimental campaign and model description

The fracture tests of the concrete TPB beams conducted by Hoover et al. [33] are simulated. The geometric dimensions, boundary conditions and loading of the concrete beam are shown in Fig. 6a. The length-to-depth ratio is $L/H = 2.4$ and the span length is $S = 2.176H$ where H denoting the beam depth varies as 40 mm, 93 mm, 215 mm and 500 mm. Three different notch-to-depth ratios, $\alpha = a_0/H$, are considered: 0.3, 0.15, and 0.075. The thickness $b = 40$mm remains constant for all the beams. The tests were performed while controlling the Crack Mouth Opening Displacement (CMOD) control.

Regarding the numerical model, the central part of the beam where fracture is expected occur is modelled as a PD-DYNA region and the remaining region as FE region, as shown in Fig. 6b. The geometric dimensions of each model, the dimensions of PD-DYNA region as well as the total number of nodes in PD and FE regions are listed in Table 1. It is important to note that the size of the models (number of nodes in the PD and FEM region) does not change for the different notch-to-depth ratio sizes. The grid spacing between the nodes in PD region and the element size in FE region are equal and specified as $\Delta = 4$mm. The grid spacing is selected based on experience from

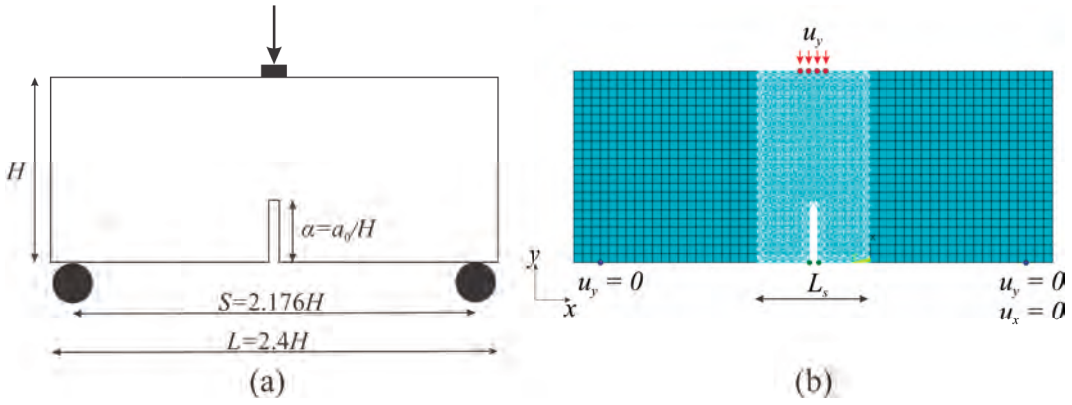

Fig. 6. Description of: a) geometry of a beam with a notch and loading conditions, and b) discretization, constraints and loading conditions in the coupled PD-DYNA/FE model (example for $H = 93$ mm and $\alpha = 0.3$).

convergence studies [32]. As shown in Fig. 6b, the displacement constraints arising from the supports are imposed as $u_x = 0$ and $u_x = u_y = 0$ on the nodes in FE region. The loading is applied as vertical displacement, u_y over a finite band of nodes (shown in red in Fig. 6b) whose depth along the beam axis is equal to the computational horizon δ_0, that is 3.015Δ. This distributed application of the boundary condition is consistent with the nonlocal nature of peridynamics and prevents artificial stress concentrations. Since the experimental reports [33] do not provide the exact width of the loading rollers and there is no evidence that they were scaled with specimen size, the same absolute loading width is used for all beam sizes. The load is computed as the reaction force at the supports, whereas the CMOD value is measured as the horizontal relative displacement of the nodes (shown in green).

The isotropic and elastic concrete has the physical and mechanical properties of $\rho = 2400\,\mathrm{kg/m^3}$, $E = 41.24$GPa, $\nu = 0.33$ and $G_f = 72.5$N/m [33,57]. It is worth noting that, in 2D plane-stress analyses, bond-based peridynamics inherently enforces a fixed Poisson's ratio of 1/3. This is a well-known theoretical limitation of the bond-based formulation, and therefore cannot be modified within PD-DYNA. Its flexural strength is $\sigma_f = 3.68$MPa for the reference beam with $H = 40$mm and $\alpha = 0.3$. In the BPD model, it is assumed that $\sigma_0 = \sigma_f$. The horizon size is $\delta_0 = 12.06$mm with a grid spacing of $\Delta = 4$mm. The micro-modulus, c is computed according to Eq.(8) or (11). Using Eq. (15), Eq. (19), Eq. (24) and Eq. (25) with $Z = 0.04$ m being the reference beam depth, the BPD parameters are calculated as $s' = s_p = 8.92 \times 10^{-5}$, $K_r = 25.56$, $\delta' = 300$mm and $n_f = 2.35$. The parameters related to the random G_f field are specified as $\ell_{cx} = \ell_{cy} = 10$mm and $CV_{Gf} = 50\%$. Four different random G_f fields are considered for each beam size.

Note that while the computational horizon$\delta_0 = 3.015\Delta$ remains constant in absolute terms for all beam sizes (since Δ is fixed), the physically relevant nonlocal length scale in the BPD model is the material characteristic horizon δ' (see Section 3.2.2). The ratio δ'/H varies with specimen size and, through the brittleness number n_f (Eq. (24), governs the ductile-to-brittle transition. The decreasing ratio δ_0/H is merely a consequence of the fixed discretization and does not introduce any spurious size effect, as verified by mesh convergence studies in [46].

4.2. Global behaviour

Fig. 7 shows the PD Force-CMOD predictions corresponding to four different random G_f fields and comparison with the experimental scatter band [58] which is obtained by retracing the external contour of the plot containing all the experimental load-CMOD curves.

Table 2 presents the predicted average flexural strength (see Eq. (2)), together with the error computed with respect to the average experimental value. It is observed that the peak loads are in good agreement with the experimental results, independent of the random G_f fields and notch-to-depth ratios. The maximum error in absolute value of the mean value of the estimated flexural strength, is equal to 14.73% when $H = 40$ mm and $\alpha = 0.3$. With respect to the softening behaviour, the predictions for $H = 40$, 93 and 215 mm fall within the experimental scatter band in practically all simulations, whereas for the $H = 500$ and α equal to 0.3 and 0.075, the results are in agreement when the CMOD values are less than 0.12 and 0.075 mm, respectively. Despites this, the trends are similar to the experimental results.

Another way to assess the global behavior of the structure and the influence of sample size is through the brittleness number, n_f, as defined in Eq. (24). The parameter,σ_0 is defined as the ultimate stress, assumed to be equal to $\sigma_{N,\mathrm{num}}$ and Z equal to H (see Table 2). As previously mentioned, structures with $n_f \leqslant 1.0$ exhibit brittle behavior, while values of $n_f \geqslant 1.5$ indicate ductile behavior. Fig. 8 presents the values of n_f for different values of α and H; the grey area marks the threshold of 1.0 and 1.5 as the ductile–brittle transition. It is evident that as α decreases and H increases, the brittleness of the structure increases, as expected. Therefore, it can be observed that for the larger samples (i.e., $H = 500$ mm), the rupture process is predominantly brittle, and as a result, the model is not able to accurately capture the post-softening behavior properly, as presented in Fig. 7.

Fig. 9 shows the predicted crack paths in each beam for the different values of notch to depth ratios. More precisely, one representative crack path for each configuration is presented. The damaged bonds (in orange) and broken ones (in red) are compared with the corresponding experimental scatter bands (black lines) [54]. It is observed that the predicted damage paths are in remarkable agreement with the experimental observations, being characterized by kinked cracks with a dominate Mode I shape.

4.3. Size effect

According to previous works [30,37,39], three mechanical properties are size dependent when three-point bending tests are employed: flexural strength, angle of rotation and fracture energy. The measure of the variation of such properties with respect to their scale is determined by the so-called fractal exponents. In the following, these exponents are computed by considering the numerical results summarized in Table 2 for the different values of notch-to-depth ratios. It is worth noting that the flexural strength, angle of

Table 1
Dimensions of the beam geometry and extent of PD region as well as the number of nodes in PD and FE regions of the model.

H (mm)	L (mm)	S (mm)	L_s (mm)	No. PD nodes	No. FE nodes
40	96	87.04	32	80	160
93	223.2	202.36	64	368	920
215	516	467.84	152	2052	4914
500	1200	1088	360	11,250	26,250

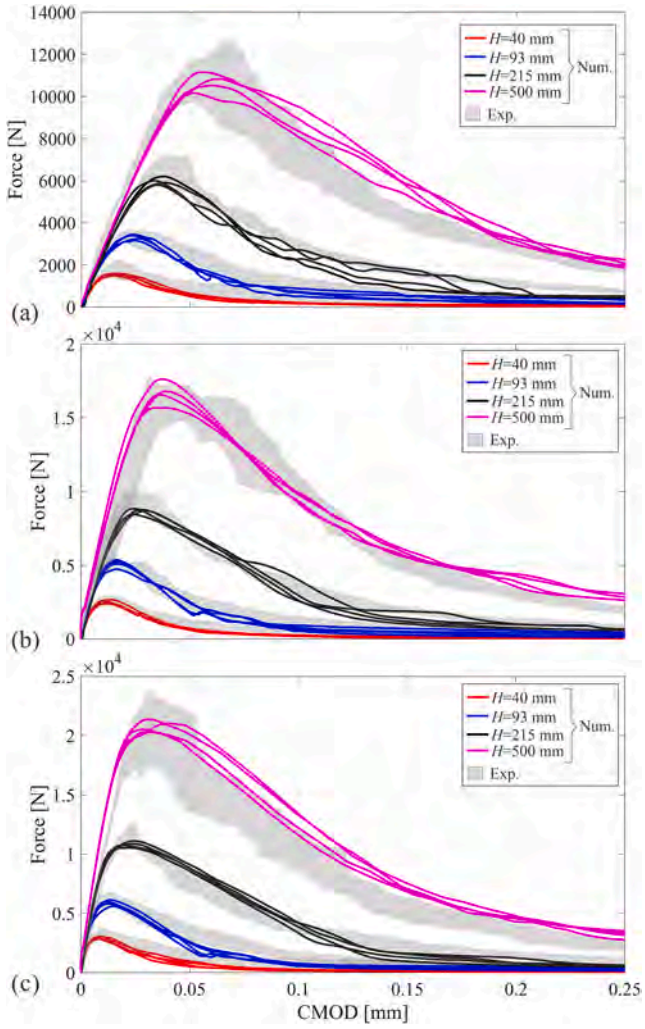

Fig. 7. Force-CMOD curves for numerical PD-DYNA simulations by varying the G_f random field, and experimental scatter band for notch to depth ratios (α) of (a) 0.3, (b) 0.15 and (c) 0.075.

rotation and fracture energy are computed according to Eqs. (2), (3) and (4), respectively.

Fig. 10 presents the numerical results showing the relationship between beam size (H) and the mechanical quantities discussed above, for different values of α. Specifically, for each quantity, the individual values (black circles), average values (red squares), and the linear approximation (solid red line) used to determine the scaling exponent are shown. Due to the scatter in the numerical results, a regression analysis was performed to estimate the confidence intervals of the exponents with 95% confidence. From the results presented in Table 3, it can be observed that the PD models are capable – regardless of the notch-to-depth ratio – of capturing the scale effect on the mechanical properties of flexural strength, critical rotation, and fracture energy. The numerically obtained values of the sum of the fractal exponents are consistent with predictions from fractal theory.

4.4. Direct fractal analysis of crack patterns

A direct geometrical analysis of the simulated crack patterns was performed to further substantiate the fractal interpretation of the size effect. According to the fractal size-effect theory [10,11], the macroscopic scaling exponent for the fracture energy, d_G, is intrinsically related to the fractal dimension D of the crack trajectory computed as $d_G = D - 1$ (for 2D problems). The analysis was carried out by considering the damage maps obtained for the beams with $\alpha = 0.075$, whose crack patterns are shown in Fig. 9. The fractal dimension D of the resulting crack path was computed through the following steps.

Crack path extraction: A simplified crack path was first extracted from each image using a custom MATLAB script. The script identifies orange and red pixels (RGB references [255 165 0] and [255 0 0] with a tolerance of $\pm$ 50) to create a binary mask of the crack region. From this mask, a single-pixel-wide path is obtained by computing, for each coordinate y, the average horizontal coordinate x of the crack pixels. This step removes thickness variations while preserving the geometric tortuosity of the crack.

Table 2
For each notch-to-depth ratio: experimental mean flexural strength ($\sigma_{N,\mathrm{exp}}$), numerical mean flexural strength ($\sigma_{N,\mathrm{num}}$) with corresponding standard deviation and the error (Er.) between this measurements; numerical critical angle rotation (ϕ_{num}) and fracture energy ($G_{f,\mathrm{num}}$) both with the corresponding standard deviations; stress brittleness number (n_f).

H (mm)	$\sigma_{N,\mathrm{exp}}$ (MPa)	$\sigma_{N,\mathrm{num}}$ (MPa)	Er. (%)	$\phi_{\mathrm{num}}.10^{-6}$ (−)	$G_{f,\mathrm{num}}$ (Nm)	n_f (−)
$\alpha = 0.3$						
40	3.68	3.19 ± 0.07	14.73	197.59 ± 19.99	76.93 ± 5.67	2.76
93	3.04	2.91 ± 0.11	4.41	129.59 ± 6.33	94.33 ± 7.72	1.95
215	2.55	2.27 ± 0.07	11.03	84.99 ± 5.28	97.79 ± 5.79	1.64
500	1.88	1.74 ± 0.09	7.46	58.16 ± 4.83	117.17 ± 4.55	1.41
$\alpha = 0.15$						
H (mm)	$\sigma_{N,\mathrm{exp}}$ (MPa)	$\sigma_{N,\mathrm{num}}$ (MPa)	Error (%)	$\phi_{\mathrm{num}}.10^{-6}$ (−)	$G_{f,\mathrm{num}}$ (Nm)	n_f (−)
40	5.38	5.17 ± 0.24	3.91	157.53 ± 23.70	84.34 ± 3.48	1.67
93	4.54	4.48 ± 0.24	1.30	87.59 ± 2.84	101.67 ± 10.1	1.27
215	3.68	3.30 ± 0.07	10.37	62.27 ± 8.08	108.09 ± 7.02	1.13
500	2.93	2.65 ± 0.08	9.41	36.56 ± 2.09	137.67 ± 9.62	0.92
$\alpha = 0.075$						
H (mm)	$\sigma_{N,\mathrm{exp}}$ (MPa)	$\sigma_{N,\mathrm{num}}$ (MPa)	Error (%)	$\phi_{\mathrm{num}}.10^{-6}$ (−)	$G_{f,\mathrm{num}}$ (Nm)	n_f (−)
40	6.69	5.94 ± 0.19	11.23	95.59 ± 14.50	84.36 ± 9.06	1.46
93	5.49	5.17 ± 0.20	5.86	69.95 ± 8.02	101.22 ± 4.19	1.10
215	4.59	4.10 ± 0.09	10.65	53.12 ± 4.32	123.48 ± 6.15	0.91
500	3.63	3.39 ± 0.08	6.56	32.26 ± 5.02	153.94 ± 4.71	0.72

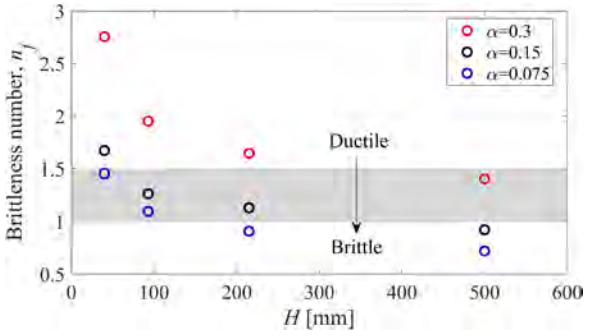

Fig. 8. Assessment of structural fragility using n_f by considering the different values of notch to depth ratios, α.

Binarization: The simplified crack path was rendered as a binary image (white pixels on black background) with a line thickness of one pixel. Small isolated pixel clusters were removed, and minor discontinuities in the crack path were closed using standard morphological operations to ensure a continuous trace for the box-counting analysis.

Box-counting: The fractal dimension D was calculated using the classical box-counting algorithm [12,59]. In this method, the image is covered with a grid of square boxes of side length r, and the number of boxes $N(r)$ that contain at least one crack pixel is counted. For a fractal object, $N(r)$ scales as r^{-D}, so D is obtained as the negative slope of the linear regression of log $N(r)$ versus log r. This technique is widely used to characterize fracture surfaces in quasi-brittle materials [59,60].

Fig. 11 presents the box-counting results for each specimen size $H = 40$, 93, 215, and 500 mm for the beams with $\alpha = 0.075$. Each subplot shows the log-log plot of $N(r) - r$ together with the linear regression used to extract D. The insets show the corresponding binarized crack paths used in the analysis. The measured fractal dimensions are $D = 1.241$, 1.270, 1.210, and 1.284 for $H = 40$, 93, 215, and 500 mm, respectively, yielding an average value of 1.25. According to the relation $d_G = D - 1$, this average corresponds to $d_G \approx 0.25$. The macroscopic exponent obtained from the scaling of G_f for this notch-to-depth ratio is $d_G = 0.24$ [0.20–0.27] (Table 3). The close agreement between the directly measured crack dimension and the macroscopic scaling exponent provides strong independent support for the fractal interpretation of the size effect in the present BPD model.

It should be noted that this direct fractal analysis was performed on a single set of crack patterns (those corresponding to $\alpha = 0.075$). Although the agreement between the measured crack dimension and the macroscopic scaling exponent is encouraging, the analysis remains limited. A more extensive investigation, including the other notch-to-depth ratios considered in this work as well as

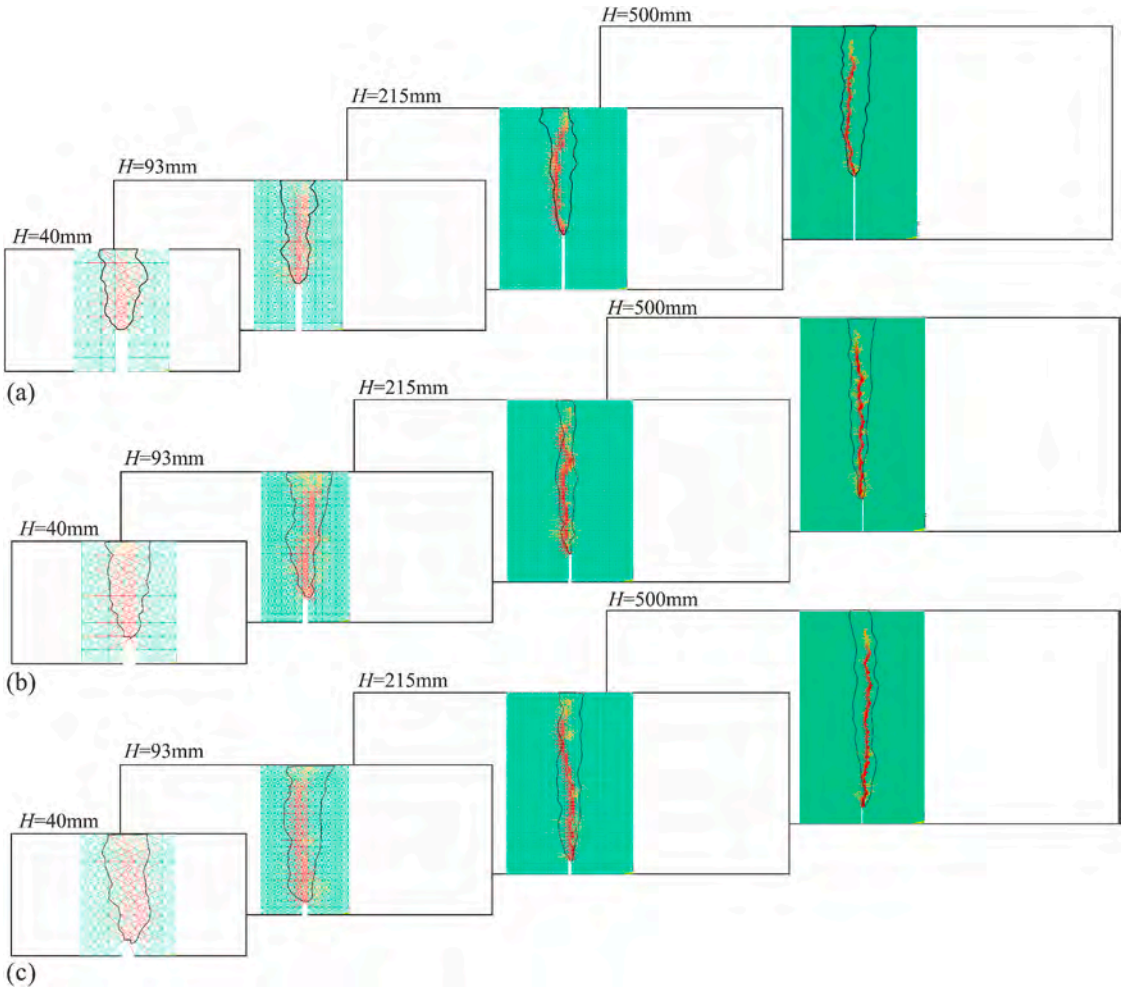

Fig. 9. Representative damage paths at failure for beams with notch-to-depth ratios of (a) 0.3, (b) 0.15, and (c) 0.075. The scatter band of the experimental crack paths (black lines) are plotted together. Note that the same grid spacing Δ was used for all specimens. As H varies, the figures are shown with different scale factors.

additional experimental and numerical datasets, is planned for future work. Such studies will help to further validate the proposed BPD framework and the PD-DYNA approach to deepen the understanding of the relationship between local crack fractality and global size-effect trends.

5. Size effect for mixed mode problems

5.1. Experimental campaign and model description

Three-point bending tests of eccentrically notched concrete beams conducted by García-Álvarez et al. [34] are simulated. The geometric dimensions, boundary conditions and loading of the concrete beam are shown in Fig. 12a. The length-to-depth ratio is $L/H = 3.125$ and the span length is $S = 2.5H$ where H denoting the beam depth varies as 80 mm, 160 mm, and 320 mm. The notch-to-depth ratio was fixed as $0.25H$, with the eccentricity-to-depth ratio β varying among 0.625, 0.3125 and 0, respectively. The thickness $b = 50$mm remains constant for all the beams. The tests were performed while controlling the Crack Mouth Opening Displacement (CMOD) control.

The numerical model is developed under plane stress conditions. The grid spacing between the nodes is specified as $\Delta = 5$mm. The number of nodes for H equal to 80, 160 and 320 mm are equal to 800, 3200 and 12800, respectively. The displacement constraints arising from the supports are imposed as $u_x = 0$ and $u_x = u_y = 0$ on the nodes, as shown in Fig. 12b. The loading is applied as vertical displacement, u_y over a finite band of nodes (shown in red in Fig. 12b). By following the same approach employed for the mode I case in Section 5.1, the depth along the beam axis is equal to the computational horizon δ_0, that is 3.015Δ, being the same absolute loading width used for all beam sizes. The load is computed as the reaction force at the supports, whereas the CMOD value is measured as the

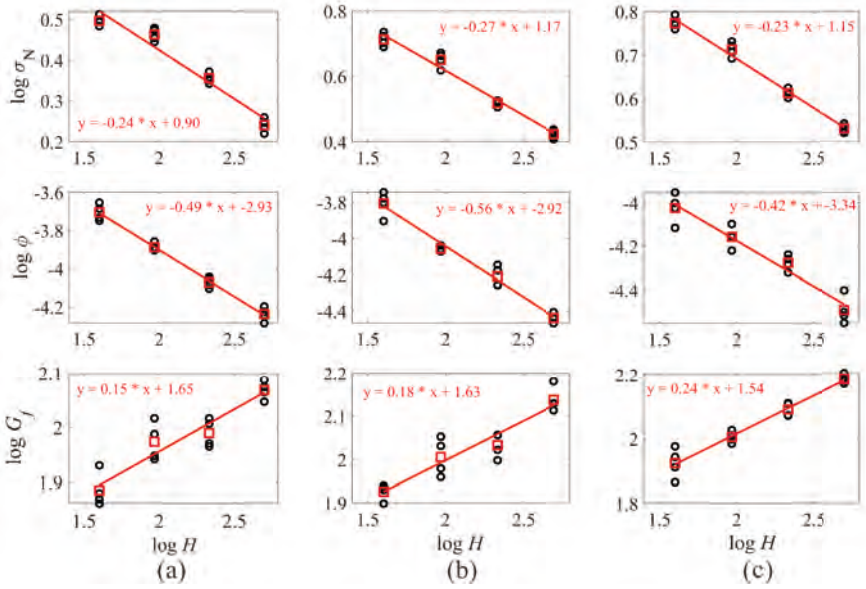

Fig. 10. Determination of the fractal exponents for the flexural strength, angle of rotation and fracture energy considering α equal to (a) 0.3, (b) 0.15, and (c) 0.075. The black circles are the individual values, the red squares the average values, and the solid red line is the linear approximation.

Table 3
Fractal exponents and the sum of them for each notch-to-depth ratios (95% confidence intervals in brackets).

α	0.3	0.15	0.075
d_σ	0.24 [0.20–0.28]	0.27 [0.24–0.30]	0.23 [0.20–0.25]
$d\chi$	0.49 [0.44–0.53]	0.56 [0.49–0.62]	0.42 [0.34–0.49]
d_G	0.15 [0.11–0.19]	0.18 [0.13–0.22]	0.24 [0.20–0.27]
$\sum d$	0.88 [0.76–0.99]	1.01 [0.86–1.14]	0.89 [0.74–1.01]

horizontal relative displacement of the nodes (shown in green).

The isotropic and elastic concrete has the physical and mechanical properties of $\rho = 2500\,\text{kg/m}^3$, $E = 33.80\,\text{GPa}$, $\nu = 0.33$ and $G_f = 125.2\,\text{N/m}$[27,57]. Its tensile strength is $\sigma_t = 3.5\,\text{MPa}$. In the BPD model, it is assumed that $\sigma_0 = \sigma_t$. The horizon size is $\delta_0 = 15.075\,\text{mm}$ with a grid spacing of $\Delta = 5\,\text{mm}$. Using Eq. (15), Eq. (19), Eq. (24) and Eq. (25) with $H = Z = 0.08\,\text{m}$ being the reference beam depth, the BPD parameters are calculated $s' = s_p = 1.04 \times 10^{-5}$, $K_r = 31.97$, $\delta' = 482$ mm and $n_f = 1.47$. The parameters related to the random G_f field are specified as $\ell_{cx} = \ell_{cy} = 5\,\text{mm}$ and $CV_{Gf} = 50\%$. Four different random G_f fields are considered for each beam size.

5.2. Global behavior

Fig. 13 shows the PD Force-CMOD predictions corresponding to four different random G_f fields and comparison with the experimental scatter band [34] which is obtained by retracing the external contour of the plot containing all the experimental load-CMOD curves.

Table 4 presents the predicted average flexural strength, together with the error computed with respect to the average experimental value. It is observed that the peak loads are in good agreement with the experimental results, independent of the random G_f fields and notch-to-depth ratios. The maximum error in absolute value of the mean value of the estimated flexural strength, is equal to 8.04% when $H = 320$ mm and $\beta = 0.625$. For some specimen sizes, the numerical curves appear to slightly underestimate the initial linear stiffness when compared with the experimental results. This difference may be associated with small mismatches between the experimental and numerical CMOD measurements. A similar trend was previously observed in phase-field simulations [57]. With respect to the softening behaviour, the predictions fall within the experimental scatter band in practically all simulations.

To assess the global behavior of the structure, the brittleness number, n_f, is computed (see Table 4) and plotted in Fig. 14 whereas the area in grey marking the ductile–brittle transition region, which lies between 1.0 and 1.5. It can be observed that the analyzed structures can be characterized as exhibiting either a ductile-type collapse or behavior within the transition zone between ductile and brittle. This explains why the softening behavior was better captured by the simulations in this case than in the one presented in the previous section.

Figs. 15 and 16 show the predicted crack paths for β equal to 0.3125 and 0.625, respectively, by varying the G_f random field (four

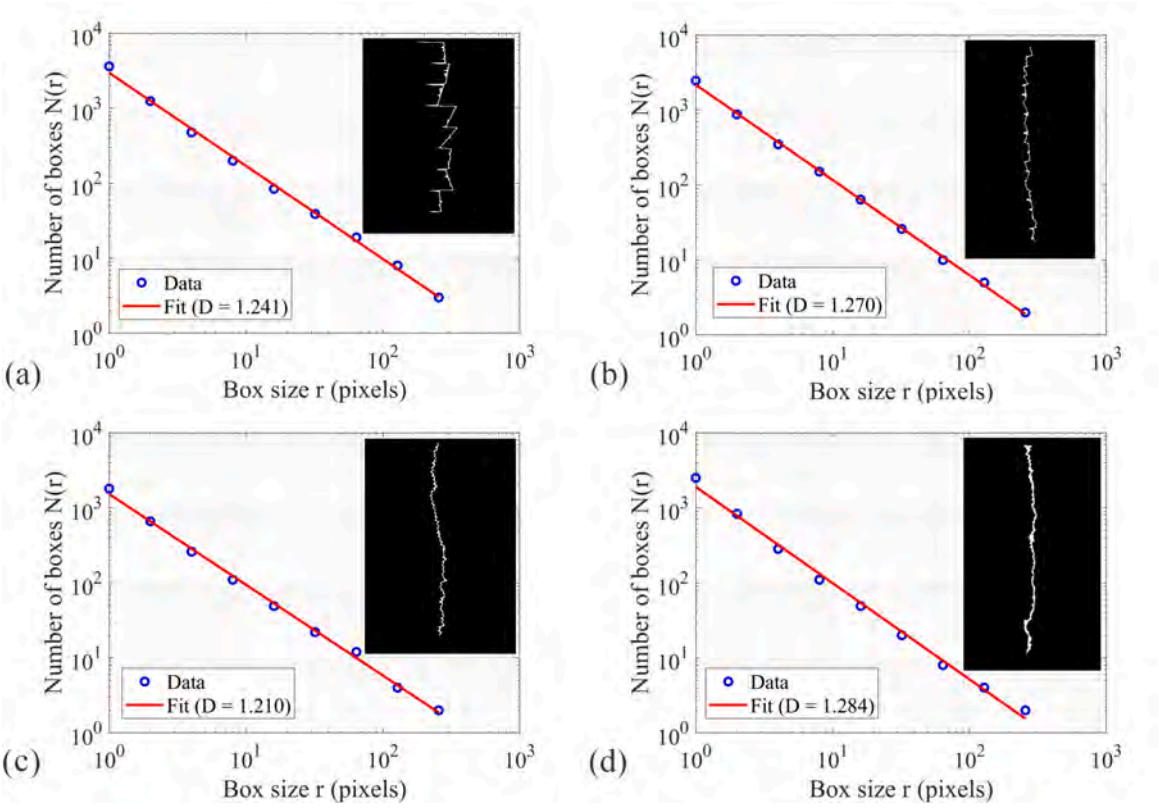

Fig. 11. Box-counting plots and binarized numerical crack paths for $\alpha = 0.075$. (a) $H = 40$ mm, (b) $H = 93$ mm, (c) $H = 215$ mm, d) $H = 500$ mm.

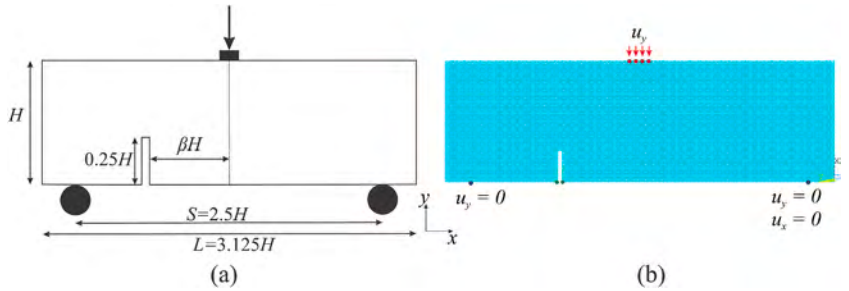

Fig. 12. Description of: (a) geometry of a beam with an eccentric notch and loading conditions, and (b) discretization, constraints and loading conditions in the PD-DYNA model (example for $H = 160$ mm and$\beta = 0.625$).

numerical simulations for each beam size were considered). Results for the mode I case ($\beta = 0.0H$) have not been included to avoid repetition. The damaged bonds (in orange) and broken ones (in red) are compared with the corresponding experimental scatter bands [34]. It is observed that the predicted damage paths are in remarkable agreement with the experimental observations. The fracture initiates from the notch and propagates at an angle towards the applied load.

5.3. Size effect

For the analysis of scale effect, the same procedure presented in Section 4.3 is applied. More precisely, the fractal exponents are computed for the flexural strength, angle of rotation and fracture energy by considering the numerical results summarized in Table 4 for the different values of notch eccentricities. Fig. 17 presents the numerical results showing the relationship between beam size (H) and the mechanical quantities presented above. The fractal exponents are summarized in Table 5; the confidence intervals of the exponents having 95% confidence are presented together in brackets. The size effect results exhibited similar trends to those observed in Section 4.3. As previously discussed, the PD models effectively captured the scale-dependent behavior of mechanical properties, with numerical values aligning well with fractal theory predictions.

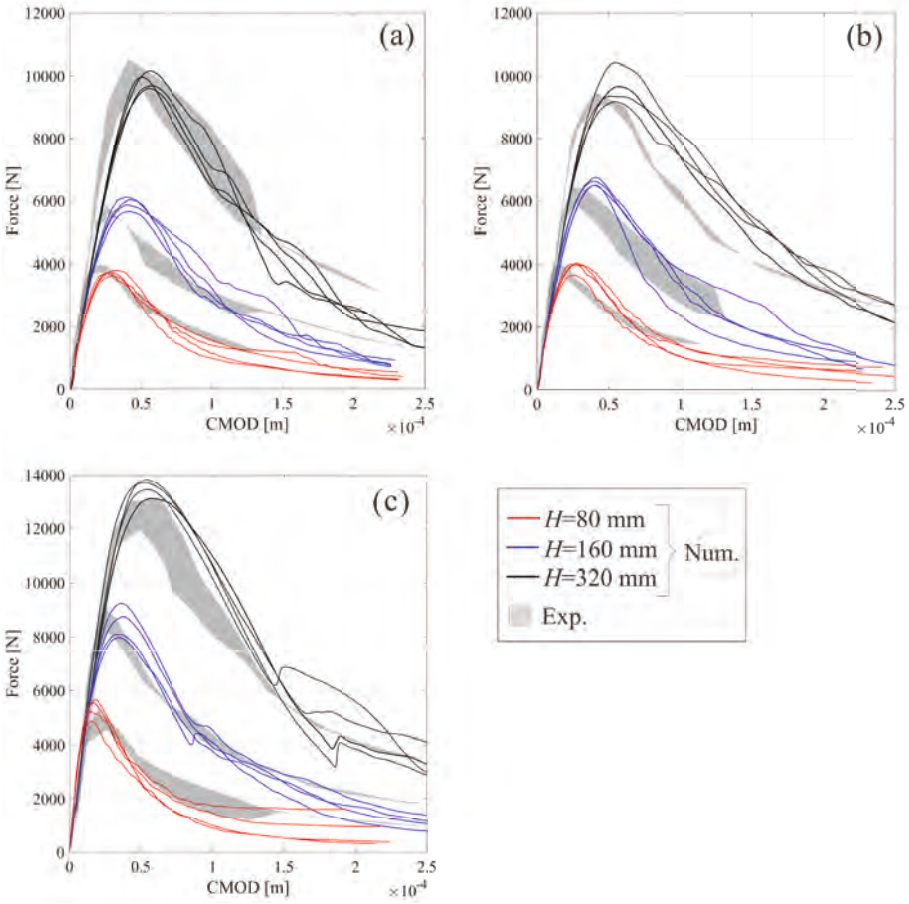

Fig. 13. Force-CMOD curves for numerical PD-DYNA simulations by varying the G_f random field, and experimental scatter band for notch eccentricity (β) of (a) 0.0, (b) 0.3125 and (c) 0.625.

Table 4
For each notch eccentricity: experimental mean flexural strength ($\sigma_{N,\text{exp}}$), numerical mean flexural strength ($\sigma_{N,\text{num}}$) with corresponding standard deviation and the error (Er.) between this measurements; numerical critical angle rotation (ϕ_{num}) and fracture energy ($G_{f,\text{num}}$) both with the corresponding standard deviations; stress brittleness number (n_f).

			$\beta = 0.0$			
H (mm)	$\sigma_{N,\text{exp}}$ (MPa)	$\sigma_{N,\text{num}}$ (MPa)	Er. (%)	$\phi_{\text{num}}.10^{-8}$ (−)	$G_{f,\text{num}}$ (Nm)	n_f (−)
80	3.61	3.49 ± 0.07	3.36	14.51 ± 1.59	112.77 ± 12.7	2.08
160	2.66	2.77 ± 0.09	4.11	10.18 ± 0.30	108.77 ± 6.46	1.86
320	2.36	2.31 ± 0.06	2.28	6.83 ± 0.40	105.79 ± 4.78	1.57
			$\beta = 0.3125$			
H (mm)	$\sigma_{N,\text{exp}}$ (MPa)	$\sigma_{N,\text{num}}$ (MPa)	Error (%)	$\phi_{\text{num}}.10^{-8}$ (−)	$G_{f,\text{num}}$ (Nm)	n_f (−)
80	3.53	3.69 ± 0.17	4.37	22.17 ± 0.64	109.42 ± 13.9	1.97
160	2.90	3.09 ± 0.06	6.49	16.71 ± 0.11	108.94 ± 14.1	1.67
320	2.17	2.26 ± 0.13	4.23	11.26 ± 0.16	114.78 ± 5.94	1.61
			$\beta = 0.625$			
H (mm)	$\sigma_{N,\text{exp}}$ (MPa)	$\sigma_{N,\text{num}}$ (MPa)	Error (%)	$\phi_{\text{num}}.10^{-8}$ (−)	$G_{f,\text{num}}$ (Nm)	n_f (−)
80	4.79	4.99 ± 0.34	4.14	26.63 ± 0.29	93.11 ± 12.11	1.46
160	4.05	3.99 ± 0.28	1.42	24.74 ± 0.12	123.64 ± 9.49	1.29
320						
2.93	3.17 ± 0.08	8.04	20.22 ± 0.12	135.14 ± 7.20	1.15	

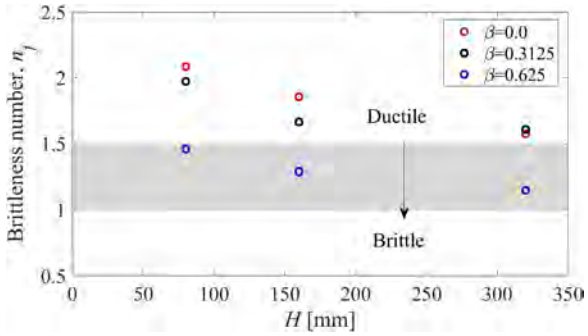

Fig. 14. Assessment of structural fragility using n_f by considering the different values of notch eccentricity, β.

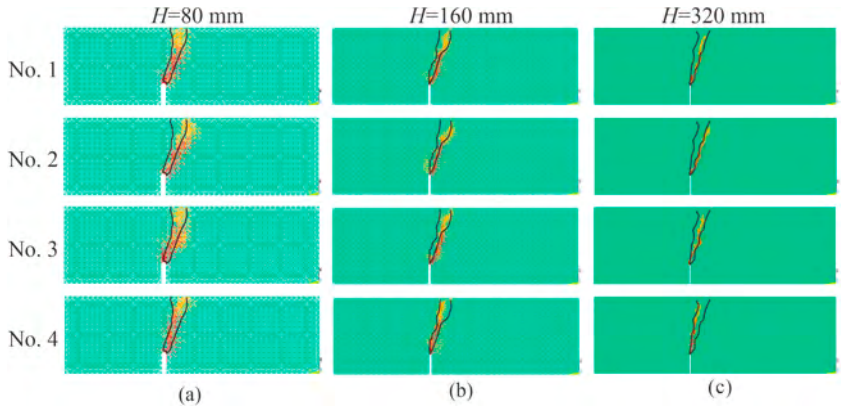

Fig. 15. Damage paths for notch eccentricity$\beta = 0.3125$ and H equal to (a) 80 mm, (b)160 mm and (c) 320 mm by varying the G_f random field. The scatter band of the experimental crack paths (black lines) are plotted together. Note that the same grid spacing Δ was used for all specimens. As H varies, the figures are shown with different scale factors.

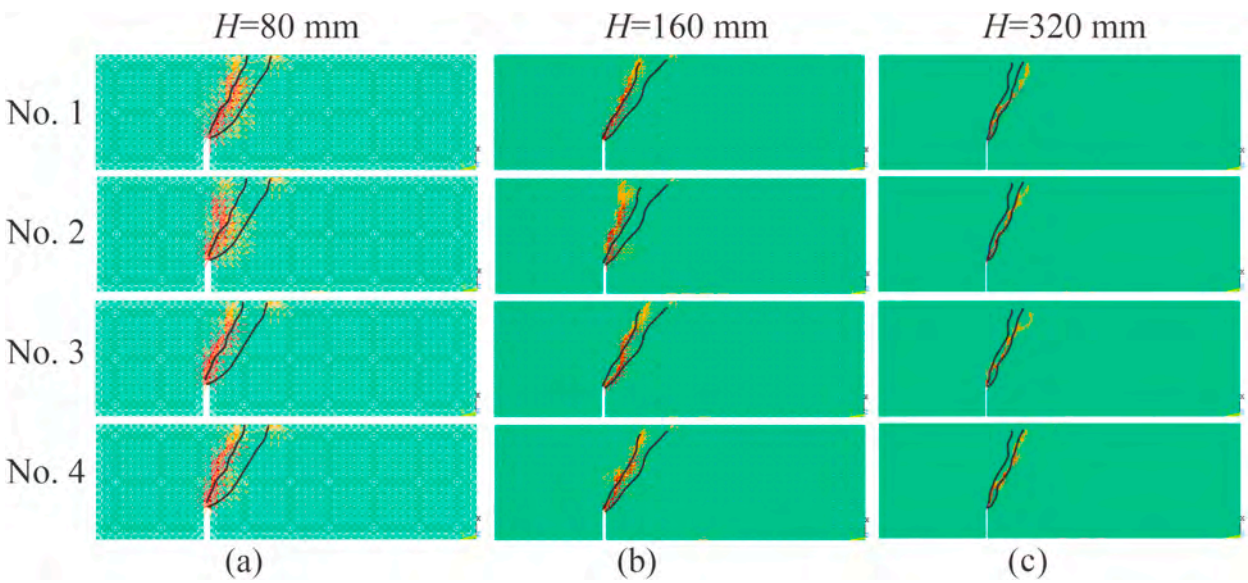

Fig. 16. Damage paths for notch eccentricity$\beta = 0.625$ and H equal to (a) 80 mm, (b)160 mm and (c) 320 mm by varying the G_f random field.. The scatter band of the experimental crack paths (black lines) are plotted together. Note that the same grid spacing Δ was used for all specimens. As H varies, the figures are shown with different scale factors.

6. Discussions

6.1. Interpretation of numerical and experimental results in the context of the fractal size effect

The numerical simulations carried out with the PD-DYNA framework, calibrated using a single set of material parameters, reproduced with high accuracy the experimental observations from both mode-I and mixed-mode three-point bending tests. For flexural strength, the average deviation between numerical and experimental peak loads was below 5%. The simulations captured the expected decrease in nominal stress with increasing beam size, in agreement with the fractal interpretation that the effective load-bearing ligament behaves as a lacunar fractal domain.

For the rotation parameter, linked to curvature within the beam span, it successfully reproduces the decreasing trend with increasing size that is consistent with the lacunar fractal representation of radial cracking patterns.

Regarding fracture energy, the predicted values accurately reflect the scaling behavior associated with invasive fractal sets such as the von Koch curve analogy. This indicates that the model not only reproduces the absolute magnitudes but also captures the size-dependent rate of variation observed experimentally.

The brittleness number also exhibited a clear size dependence. Smaller specimens showed lower brittleness, reflecting a more ductile-like response, whereas larger specimens approached a more brittle behaviour. This transition was accurately reproduced by the PD-DYNA simulations, further supporting the capability of the model to capture not only global strength and energy dissipation, but also the shift in fracture mode from ductile to brittle with increasing size.

In addition to the global mechanical parameters and behaviour, the PD-DYNA simulations reproduced the crack trajectories observed experimentally in both mode-I and mixed-mode tests. In mode I, cracks propagated along paths close to the mid-plane, while in mixed-mode conditions the model captured the kinked and tortuous paths characteristic of quasi-brittle fracture under combined loading. This agreement indicates that the implemented bilinear PD model, the 3D stochastic field and the attenuation kernel are capable of representing the local stress redistributions and microstructural heterogeneities that govern crack deflection and branching. Such capability is critical for accurately predicting the size effect, as the tortuosity of the fracture path can influence the effective fracture surface and, consequently, the scaling behaviour.

It is important to distinguish between the two horizon scales present in the BPD model when interpreting the size effect. The computational horizon $\delta_0 = 3.015\Delta$ is a model parameter that defines the integration domain of the peridynamic equations. Because a constant grid spacing Δ is used for all specimen sizes, the ratio δ_0/H decreases as H increases. However, this variation does not imply a change in the physical degree of nonlocality. The intrinsic material length scale is the characteristic horizon $\delta^{'}$, which is a material constant derived from the brittleness number and the material properties (Section 3.2.2). The physically relevant ratio governing the size effect is $\delta^{'}/H$, which decreases with H and drives the ductile-to-brittle transition captured by the brittleness number n_f. The BPD model is constructed such that, through the parameter K_r (Eq. (19), the macroscopic response is independent of the specific value of δ_0, as confirmed by mesh convergence studies [46]. Therefore, the observed scaling of strength, rotation, and fracture energy with specimen size is a genuine physical size effect, not an artefact of the evolving δ_0/H ratio.

Finally, it is also worth emphasising the distinct roles played by the material characteristic horizon $\delta^{'}$ and the random G_f field in capturing the size effect. The parameter $\delta^{'}$ defines the intrinsic material length scale and controls the deterministic size effect governing the ductile-to-brittle transition, as characterized by the brittleness number n_f. In contrast, the random field introduces statistical variability, giving rise to the scatter observed in experimental data and to the realistic tortuosity of crack paths. The random field alone, would be insufficient to reproduce the correct mean scaling behaviour. The interaction of deterministic material length scale and stochastic description of local toughness is essential for the BPD model to capture both the average size-effect trends and the inherent randomness of quasi-brittle fracture.

6.2. Dimensional framework for extrapolating the fractal law using BPD model parameters

The dimensional analysis presented here follows the framework previously introduced in [30], which established how the parameters of the BPD model can be combined into dimensionless groups to describe the fractal size effect. In the present work, this methodology is briefly described and applied to the PD-DYNA simulations, enabling direct extrapolation of the results to structural sizes beyond those tested experimentally. As demonstrated in [30], this framework not only links the BPD parameters to the fractal exponents but also predicts the asymptotic behavior for very small and very large structural sizes, Table 6. To complement this, Fig. 18 (adapted from [30]) schematically illustrates the variation of each property, highlighting the transitional zone governed by the fractal law and the asymptotic regimes where classical strength or LEFM criteria dominate. It is worth noting that the parameters listed in Table 6 were originally defined for uniaxial tensile tests in [30]. Nevertheless, the same dimensional framework can be extended to other mechanical properties affected by the size effect, including those obtained from three-point bending tests – the main focus of the present study. The specific comments are the following:

(1) The trends of the tensile strength scaling law (Fig. 18a) indicate that for smaller samples, a homogeneous regime should be assumed, where there is no variation of the strength with respect to the dimensions of the sample ($d\sigma_u = 0.0$). On the other hand, for larger samples, it is evident that the material strength is governed by the LEFM, resulting in a scaling exponent ($d\sigma_u$) equal to 0.5.

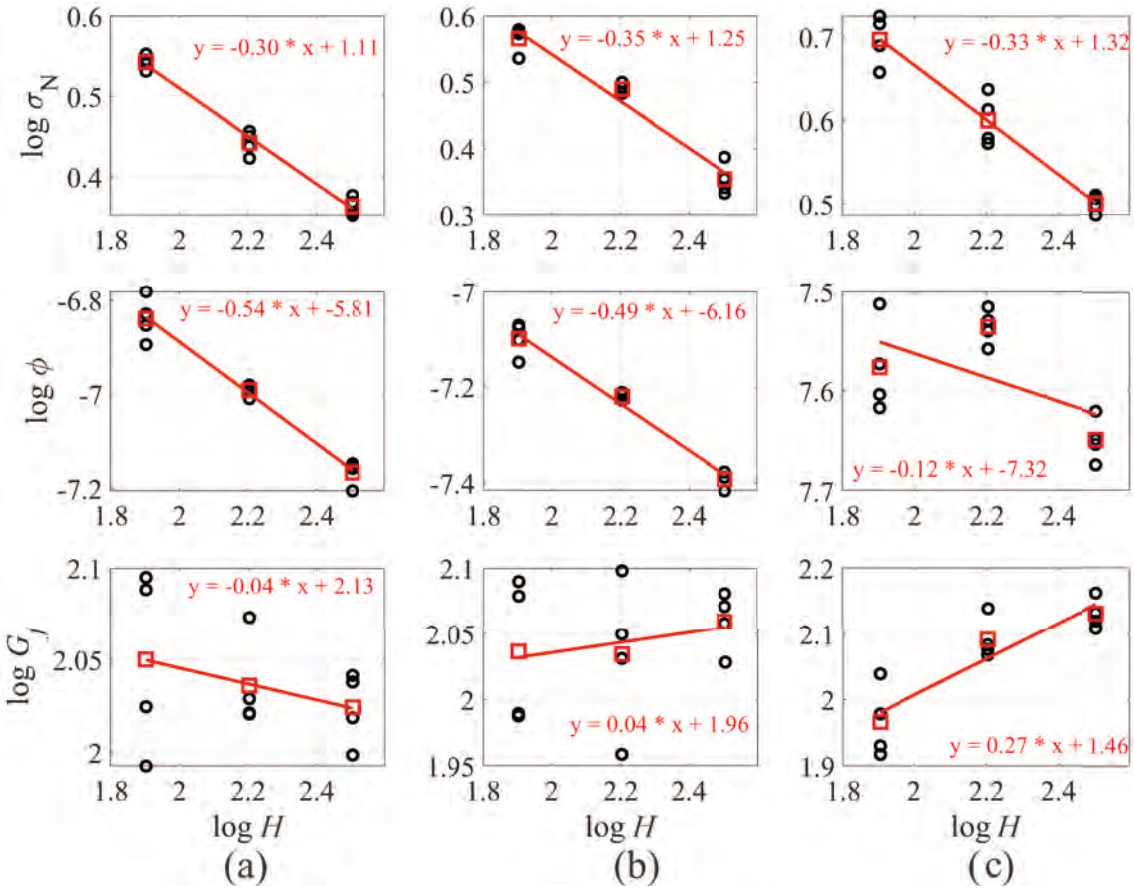

Fig. 17. Determination of the fractal exponents for the flexural strength, angle of rotation and fracture energy considering β equal to (a) 0.0, (b) 0.3125, and (c) 0.625. The black circles are the individual values, the red squares the average values, and the solid red line is the linear approximation.

Table 5
Fractal exponents and the sum of them for each notch eccentricity (95% confidence intervals in brackets).

β	0.0	0.3125	0.625
d_σ	0.30 [0.26–0.33]	0.35 [0.29–0.41]	0.33 [0.26–0.39]
d_χ	0.54 [0.45–0.62]	0.49 [0.42–0.55]	0.12 [0.01–0.25]
d_G	0.04 [0.04–0.12]	0.04 [0.00–0.15]	0.27 [0.16–0.38]
$\sum d$	0.87 [0.75–1.07]	0.84 [0.79–1.11]	0.72 [0.43–1.02]

(2) Fig. 18b shows the trends of the fracture energy scaling law, whereas Fig. 18c shows a schematic representation of the fracture energy scaling law taking into account different body sizes, H, under a given boundary condition and loading (q_c). The representation of the CTOD is presented as well. More precisely, for samples of a relatively small size, the CTOD value is proportional to the sample size, H, therefore, $d_G = 1.0$. This means that for any small body with a crack (which will appear at the moment of fracture), the CTOD, and consequently the critical crack size, is restricted to size of the sample. On the other hand, for large samples, the CTOD, and consequently the critical crack size, are governed by material charactistic length, that is δ', and therefore constant, that is $d_G = 0.0$ (see Fig. 18b).

(3) Dimensional analysis yields the critical strain/rotation scaling shown in Fig. 18a. In the limit as $H \to 0$, a homogeneous regime is expected and deformation is diffuse throughout the body, so no size effect arises: $d\varepsilon_u = 0.0$. In the opposite limit, $H \to \infty$ the response up to peak stress follows the LEFM, and the size effect follows the same trend, giving $d\varepsilon_u = 0.5$.

The asymptotic scaling trends derived from the dimensional framework are consistent with results reported in the literature. For instance, Wang et al. [4] (see Fig. 19) shows a very similar transition pattern for flexural strength and fracture energy when extrapolating specimen sizes from laboratory to structural scales. Although the underlying modeling strategies differ from the present fractal-based approach, the overall convergence of results toward the same size-dependent limits supports the robustness of the scaling

Table 6
Asymptotic behavior and dimensional scaling relations of mechanical quantities based on the BPD model. See [30] for details.

Mechanical Quantity	Tensile strength (σ_u)	Fracture energy (G_f)	Critical strain (ε_u)
Dimensional form	$\sigma_u = C_{\sigma u} E \left(\frac{G_f}{EH}\right)^{\alpha_1} \left(\frac{\delta}{H}\right)^{\alpha_2}$	$G_f = EHC_{Gf} \left(\frac{G_f}{EH}\right)^{\beta_1} \left(\frac{\delta}{H}\right)^{\beta_2}$	$\varepsilon_u = C_{\varepsilon u} \left(\frac{G_f}{EH}\right)^{\gamma_1} \left(\frac{\delta}{H}\right)^{\gamma_2}$
Exponents ($H \to 0$)	$\alpha_1 = 0.5$ and $\alpha_2 = -0.5$	$\beta_1 = 1.0$ and $\beta_2 = -1.0$	$\gamma_1 = 0.5$ and $\gamma_2 = -0.5$
Small-scale regime ($H \to 0$)	$\sigma_u \propto H^{0.0}$ Constant – no size effect	$G_f \propto H^{1.0}$ CTOD scales with specimen size	$\varepsilon_u \propto H^{0.0}$ Constant – diffuse strain across specimen
Exponents ($H \to \infty$)	$\alpha_1 = 0.5$ and $\alpha_2 = 0.0$	$\beta_1 = 1.0$ and $\beta_2 = 0.0$	$\gamma_1 = 0.5$ and $\gamma_2 = 0.0$
Large-scale regime ($H \to \infty$)	$\sigma_u \propto H^{-0.5}$ LEFM regime	$G_f \propto H^{0.0}$ Constant – independent of specimen size (LFEM)	$\varepsilon_u \propto H^{-0.5}$ matches σ_u scaling (LEFM)
Scaling exponent (d)	$d\sigma_u = 0.0 \to 0.5$	$d_G = 1.0 \to 0.0$	$d\varepsilon_u = 0.0 \to 0.5$

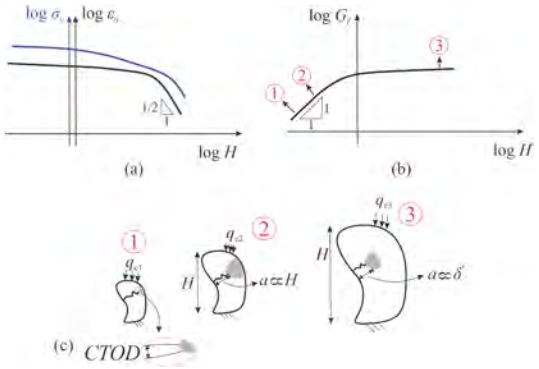

Fig. 18. Scaling laws derived from the dimensional analysis of the BPD model parameters. (a) Tensile strength and critical strain and (b) fracture energy. (c) Schematic representation of the fracture energy scaling law (
adapted from [30]).

law interpretation.

6.3. Implications and limitations

The integration of PD-DYNA with a fractal-based interpretation of the size effect offers a predictive modeling tool that is both physically grounded and numerically robust. By incorporating material heterogeneity through stochastic fields, a spatial attenuation kernel, and a discretized micro-modulus function, the present approach overcomes limitations observed in earlier PD studies, such as difficulty in reproducing transitional size effects.

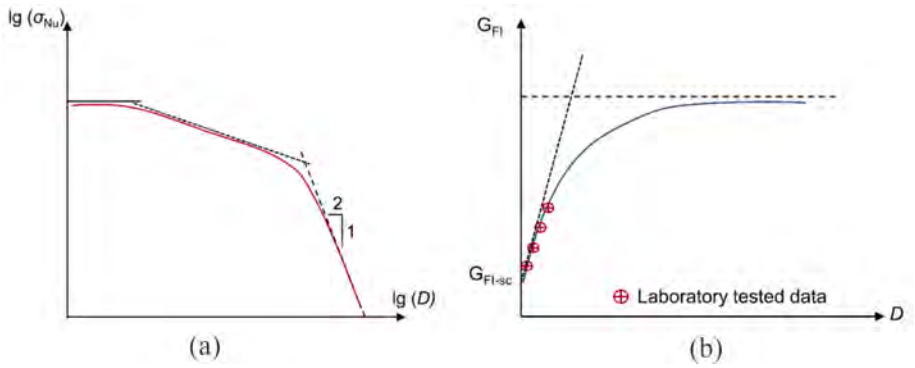

Fig. 19. Size effect model (a) for nominal strength and (b) fracture energy proposed by Wang et al. [4] (
adapted from [4]).

From a practical standpoint, this framework enables structural engineers to estimate the fracture behavior of quasi-brittle materials across a wide size range, significantly reducing the need for costly full-scale testing. Moreover, the explicit connection between PD parameters and fractal exponents provides a clear path for interpreting simulation outputs in terms of measurable physical quantities.

Nevertheless, some limitations remain. The main challenge lies in the high computational cost of fully three-dimensional simulations, even when PD is coupled with FEM. This restricts the applicability of the method to very large-scale structural problems, where fine discretization becomes prohibitive. Future work should therefore focus on strategies to mitigate this limitation, such as hybrid multiscale frameworks (employing PD only in localized fracture regions), adaptive horizon formulations, or exploiting high-performance computing architectures including GPU-based parallelization.

7. Conclusions

This study examined the size-dependent fracture behavior of quasi-brittle materials using a PD framework implemented in LS-DYNA and interpreted via a fractal-based scaling law. A bilinear PD model – augmented with a 3D stochastic field, a spatial attenuation kernel, and a discretized micromodulus function – was employed to capture material heterogeneity and structural scaling. The formulation was validated against three-point bending experiments on notched beams under mode I and mixed-mode loading. Key contributions can be summarized as:

- A native Ansys PD–LS-DYNA integration (PD-DYNA) delivering a practical, scalable computational framework for engineering applications.
- Accurate reproduction of peak loads, softening responses, and tortuous crack paths observed in laboratory tests using a single, consistent parameter set.
- A unified, physically grounded interpretation of flexural strength, fracture energy, and rotation/curvature across specimen sizes by coupling PD results with the fractal size-effect framework.
- A pathway to extrapolate laboratory-scale findings to real structural dimensions by linking peridynamic parameters to measurable fractal exponents, reducing reliance on prohibitively costly full-scale testing.

Overall, the results demonstrate that PD-DYNA, combined with a fractal interpretation of size effects, is a reliable and versatile tool for modeling quasi-brittle fracture. Future work should address the computational demands of fully 3D simulations, explore alternative PD kernels, and broaden validation to other quasi-brittle materials and loading scenarios.

CRediT authorship contribution statement

Leandro F. Friedrich: . **Vicente B. Puglia:** . **Angélica B. Colpo:** . **Ignacio Iturrioz:** Writing – review & editing, Supervision, Methodology, Formal analysis. **Giuseppe Lacidogna:** Writing – review & editing, Supervision, Formal analysis. **Erdogan Madenci:** Writing – review & editing, Supervision, Methodology, Formal analysis.

Declaration of competing interest

The authors declare that they have no known competing financial interests or personal relationships that could have appeared to influence the work reported in this paper.

Acknowledgments

The authors wish to acknowledge the Brazilian National Council for Scientific and Technological Development (CNPq) and the Coordination for the Improvement of Higher Level of Education Personnel (CAPES). The sponsorship guaranteed with basic research funds provided by Politecnico di Torino, Italy, for their support in this work is acknowledged.

Data availability

Data will be made available on request.

References

[1] Bažant ZP. Size effect in blunt fracture: concrete, rock, metal. J Engng Mech 1984;100:518–35.
[2] Taylor, D. (2007). The theory of critical distances: A new perspective in fracture mechanics. Elsevier.
[3] Van Mier, J. G. M. (1996). Fracture processes of concrete. CRC Press. https://doi.org/10.1201/b22384.
[4] Wang Q, Li Q, Yin X, Xu S. Structural size effect in the mode I and mixed mode I/II fracture of strain-hardening cementitious composites (SHCC). Int J Solids Struct 2024;288:112628. https://doi.org/10.1016/j.ijsolstr.2023.112628.
[5] Hu X, Duan K. Size effect and quasi-brittle fracture: the role of FPZ. Int J Fract 2008;154:3–14. https://doi.org/10.1007/s10704-008-9290-7.
[6] Bažant ZP, Planas J. Fracture and size effect in concrete and other quasibrittle materials. Routledge 1998. https://doi.org/10.1201/9780203756799.
[7] Hoover CG, Bažant ZP. Cohesive crack, size effect, crack band and work-of-fracture models compared to comprehensive concrete fracture tests. Int J Fract 2014; 187:133–43. https://doi.org/10.1007/s10704-013-9926-0.

[8] Morel S, Dourado N. Size effect in quasibrittle failure: Analytical model and numerical simulations using cohesive zone model. Int J Solids Struct 2011;48:1403–12. https://doi.org/10.1016/j.ijsolstr.2011.01.014.
[9] Wang Q, Li Q, Yin X, Xu S, Su Z, Xie H. Fracture behavior and size effect of UHPFRC: Experimental and meso-scale numerical investigation. Engng Fract Mech 2023;283:109197. https://doi.org/10.1016/j.engfracmech.2023.109197.
[10] Carpinteri A, Chiaia B, Ferro G. Size effects on nominal tensile strength of concrete structures: Multifractality of material ligaments and dimensional transition from order to disorder. Mater Struct 1995;28:311–7. https://doi.org/10.1007/BF02473145.
[11] Carpinteri, A., Chiaia, B., & Ferro, G. (1995). Multifractal scaling law: An extensive application to nominal strength size effect of concrete structures. Atti del Dipartimento di Ingegneria Strutturale, 50. Politecnico di Torino.
[12] Mandelbrot BB, Wheeler JA. The fractal geometry of nature. Am J Phys 1983;51(3):286–7. https://doi.org/10.1119/1.13295.
[13] Wu JY, Yao JR. A model scaling approach for fracture and size effect simulations in solids: Cohesive zone, smeared crack band and phase-field models. Comput Methods Appl Mech Engng 2022;400:115519. https://doi.org/10.1016/j.cma.2022.115519.
[14] Barenblatt GI. The formation of equilibrium cracks during brittle fracture: General ideas and hypotheses. Axially-symmetric cracks. J Appl Math Mech 1959;23:622–36.
[15] Hillerborg A, Modéer M, Petersson P. Analysis of crack formation and crack growth in concrete by means of fracture mechanics and finite elements. Cem Concr Res 1976;6:773–81.
[16] Bažant ZP, Oh BH. Crack band theory for fracture of concrete. Mater Struct 1983;16:155–77.
[17] Rashid Y. Analysis of prestressed concrete pressure vessels. Nucl Engng Des 1968;7:334–44.
[18] Oliver J. A consistent characteristic length for smeared cracking models. Int J Numer Meth Engng 1989;28:461–74.
[19] Belytschko T, Black T. Elastic crack growth in finite elements with minimal remeshing. Int J Numer Meth Engng 1999;45(5):601–20. https://doi.org/10.1002/(SICI)1097-0207(19990620)45:5.
[20] Francfort GA, Marigo JJ. Revisiting brittle fracture as an energy minimization problem. J Mech Phys Solids 1998;46(8):1319–42. https://doi.org/10.1016/S0022-5096(98)00034-9.
[21] Wu J-Y, Yao J-R, Le J-L. Phase-field modeling of stochastic fracture in heterogeneous quasi-brittle solids. Comput Methods Appl Mech Engng 2023;416:116332. https://doi.org/10.1016/j.cma.2023.116332.
[22] Nikolić M, Karavelić E, Ibrahimbegović A, Miščević P. Lattice element models and their peculiarities. Arch Comput Meth Engng 2018;25(3):753–84. https://doi.org/10.1007/s11831-017-9210-y.
[23] Rios JD, Riera JD. Size effects in the analysis of reinforced concrete structures. Engng Struct 2004;26:1115–25.
[24] Kosteski LE, Iturrioz I, Lacidogna G, Carpinteri A. Size effect in heterogeneous materials analyzed through a lattice discrete element method approach. Engng Fract Mech 2020;232:107041. https://doi.org/10.1016/j.engfracmech.2020.107041.
[25] Kosteski LE, Iturrioz I, Friedrich LF, Lacidogna G. A study by the lattice discrete element method for exploring the fractal nature of scale effects. Sci Rep 2022;12:20137. https://doi.org/10.1038/s41598-022-20137-3.
[26] Silling SA. Reformulation of elasticity theory for discontinuities and long-range forces. J Mech Phys Solids 2000;48:175–209.
[27] Hobbs M, Dodwell T, Hattori G, Orr J. An examination of the size effect in quasi-brittle materials using a bond-based peridynamic model. Engng Struct 2022;262:114207.
[28] Bažant ZP, Nguyen HT, Dönmez AA. Critical comparison of Phase-Field, Peridynamics, and Crack Band Model M7 in light of Gap Test and classical fracture tests. J Appl Mech 2022;89(6):061008.
[29] Bazilevs, Y., Behzadinasab, M., & Foster, J. T. (2022) Simulating concrete failure using the microplane (M7) constitutive model in correspondence-based peridynamics: Validation for classical fracture tests and extension to discrete fracture. *Journal of the Mechanics and Physics of Solids*, *166*, 104947.
[30] Friedrich LF, Kosteski LE, Cezar ÉS, Colpo AB, Bremm C, Lacidogna G, et al. A fractal analysis of the size effect in quasi-brittle materials: Experimental tests and peridynamic simulations. Mathematics 2025;13(1):94. https://doi.org/10.3390/math13010094.
[31] Ren B, Wu CT, Askari E. A 3D discontinuous Galerkin finite element method with the bond-based peridynamics model for dynamic brittle failure analysis. Int J Impact Eng 2017;99:14–25.
[32] Friedrich LF, Puglia VB, Colpo AB, Pinto AVG, Iturrioz I, Madenci E. Implementation of bond-based peridynamics in ANSYS LS-DYNA for brittle and quasi-brittle material failure analysis. Mech Adv Mater Struct 2025;1–20. https://doi.org/10.1080/15376494.2025.2490816.
[33] Hoover CG, Bažant ZP. Comprehensive concrete fracture tests: size effects of Types 1 & 2, crack length effect and postpeak. Engng Fract Mech 2013;110:281–9.
[34] Grégoire D, Rojas-Solano L, Pijaudier-Cabot G. Failure and size effect for notched and unnotched concrete beams. Int J Numer Anal Meth Geomech 2013;37:1434–52.
[35] Carpinteri A. Scaling laws and renormalization groups for strength and toughness of disordered materials. Int J Solids Struct 1994;31:291–302. https://doi.org/10.1016/0020-7683(94)90107-4.
[36] Borodich FM. Fractals and fractal scaling in fracture mechanics. Int J Fract 1999;95:239–59. https://doi.org/10.1023/A:1018660604078.
[37] Lacidogna G, Piana G, Accornero F, Carpinteri A. Multi-technique damage monitoring of concrete beams: acoustic emission, digital image correlation, dynamic identification. Constr Build Mater 2020;242:118114.
[38] JCI-S-001, 2003. Method of Test for Fracture Energy of Concrete by use of Notched Beam, Japan Concrete Institute, Tokyo, Japan.
[39] Carpinteri A, Accornero F. Rotation Versus Curvature Fractal Scaling in Bending failure. Phys Mesomech 2019;22:46–51. https://doi.org/10.1134/S1029959919010089.
[40] Silling SA, Askari E. A meshfree method based on the peridynamic model of solid mechanics. Comput Struct 2005;83:1526–35.
[41] Madenci, E. & Oterkus, E. (2014). Peridynamic theory and its applications. Springer, New York. https://doi.org/10.1007/978-1-4614-8465-3.
[42] Gu X, Zhang Q, Huang D, Yu YT. Wave dispersion analysis and simulation method for concrete SHPB test in peridynamics. Engng Fract Mech 2016;160:124–37.
[43] Gu X, Zhang Q. A modified conjugated bond-based peridynamic analysis for impact failure of concrete gravity dam. Meccanica 2020;55(3):547–66.
[44] Kilic B, Madenci E. Prediction of crack paths in a quenched glass plate by using peridynamic theory. Int J Fract 2009;156(2):165–77.
[45] Huang D, Lu GD, Qiao PZ. An improved peridynamic approach for quasi-static elastic deformation and brittle fracture analysis. Int J Mech Sci 2015;94:111–22.
[46] Friedrich LF, Colpo AB, Kosteski LE, Vantadori S, Iturrioz I. A novel peridynamic approach for fracture analysis of quasi-brittle materials. Int J Mech Sci 2022;227:107445.
[47] Cabral NR, Invaldi MA, D'Ambra RB, Iturrioz I. An alternative bilinear peridynamic model to simulate the damage process in quasi-brittle materials. Engng Fract Mech 2019;216:106508. https://doi.org/10.1016/j.engfracmech.2019.106508.
[48] Friedrich LF, Iturrioz I, Colpo AB, Vantadori S. Fracture failure of quasi-brittle materials by a novel peridynamic model. Compos Struct 2023;323:117402.
[49] Friedrich LF, Colpo AB, Iturrioz I, Zanichelli A, Vantadori S. A novel non-linear peridynamic model for quasi-brittle materials under cyclic loading. Engng Fract Mech 2024;306:110181. https://doi.org/10.1016/j.engfracmech.2024.110181.
[50] D. Taylor, The Theory of Critical Distances: A New Perspective in Fracture Mechanics, Elsevier, Amsterdam, 2007.
[51] Tanzi BNR, Birck G, Sobczyk M, Iturrioz I, Lacidogna G. Truss-like discrete element method applied to damage process simulation in quasi-brittle materials. Appl Sci 2023;13:5119. https://doi.org/10.3390/app13085119.
[52] Carpinteri A, Marenga C, Savadori A. Ductile-brittle transition by varying structural size. Engng Fract Mech 1985;21(2):263–71.
[53] Gao H. Application of fracture mechanics concepts to hierarchical biomechanics of bone and bone-like materials. Int J Fract 2006;138:101–37. https://doi.org/10.1007/s10704-006-7156-4.
[54] ANSYS. (2013). ANSYS LS-DYNA user's guide (Version 15.0) [Computer software manual].
[55] Parks ML, Seleson P, Plimpton SJ, Lehoucq RB, Silling SA. Peridynamics with LAMMPS: a user guide v0.2 beta. Sandia National Laboratories 2010.
[56] Colpo A, Vantadori S, Friedrich L, Zanichelli A, Ronchei C, Scorza D, et al. A novel LDEM formulation with crack frictional sliding to estimate fracture and flexural behaviour of the shot-earth. Compos Struct 2023;305:116514.
[57] Feng D, Wu J. Phase-field regularized cohesive zone model (CZM) and size effect of concrete. Engng Fract Mech 2018;197:66–79.

[58] Wendner R, Vorel J, Smith J, et al. Characterization of concrete failure behavior: a comprehensive experimental database for the calibration and validation of concrete models. Mater Struct 2015;48:3603–26.
[59] Carpinteri A, Chiaia B. Multifractal nature of concrete fracture surfaces and size effects on nominal fracture energy. Mater Struct 1995;28(8):435–43. https://doi.org/10.1007/BF02473162.
[60] Carpinteri A, Cornetti P, Puzzi S. Morphological fractal dimension versus power-law exponent in the scaling of damaged media. Int J Damage Mech 2009;18(3):259–82. https://doi.org/10.1177/1056789508098700.